Quarterly Report for

Contract DE-FG36-02ID14418

Stanford Geothermal Program

April-June 2005

Table of Contents

1. MEASUREMENTS OF IN-SITU WATER SATURATION IN GEOTHERMAL ROCKS

This research project is being conducted by Research Assistant Aysegul Dastan, Senior Research Engineer Kewen Li, and Prof. Roland Horne. The objective is to study the effects of pressure, temperature and permeability on in-situ water saturation in geothermal reservoirs.

1.1 OUTLINE

Experimental characterization of geothermal rocks is essential for the estimation of the capacity of geothermal reservoirs. The basic components of a geothermal reservoir are its reserves of steam and immobile water. Knowledge of immobile and in-situ water saturation as well as porosity provides a better understanding of the field and its exploitative capacity. Usually numerical simulations based on field measurements are used for this purpose. However, it is also possible and very useful to make direct measurements of the irreducible water saturation in core samples from the reservoir of interest. That way, a direct comparison can be made with the inferred water saturation from simulations.

As part of an earlier California Energy Commission (CEC) project, The Geysers geothermal field in Northern California was studied (Horne, 2003). In that work, both numerical simulations and direct measurements were compared. The project developed an X-ray CT method for the direct measurement of the water saturation and the porosity of a core sample from The Geysers area. The results obtained were preliminary, because only a limited number of experiments could be conducted at that time.

The objective in this project is to extend the method of direct measurement. First, we have developed a new procedure to systematically characterize the rocks. This development uses the previously-characterized Geysers rock. In this report, we first introduce the parameters we would like to measure and our methodology for experimental characterization. Next, we will summarize our accomplishments so far. Finally, we will discuss future steps.

In the previous report we focused mostly on analyzing and modifying the experimental apparatus such that all possible mechanisms that may result in inaccurate measurements could be eliminated. We analyzed the experimental apparatus that was used previously component by component and made the necessary adjustments to ensure robustness of the equipment. That report of Winter 2005 also described a comprehensive procedure to detect the locations of leaks, including the ones that are not readily observable.

In this report we focus on (1) calculation of permeability using the pressure pulse decay method, and (2) preliminary CT scanning of the sample. Also, we have modified the existing procedure for the measurements. We plan to obtain the complete results in the quarter to come, and repeat the already verified procedure with other geothermal rocks. We would like to analyze the data; an in particular we would like to investigate the suprosingly large irreducible water saturation and if confirmed, its possible consequences.

1.1.1 Characterization of the rocks: S_w and ϕ parameters

As we summarized in our previous reports, characterization examines the computer tomography (CT) images of the rock sample. The objective is to determine experimentally the saturation and porosity values, represented by S_w and ϕ, respectively. The CT scanner scans the sample and measures the distribution of water in the sample. Hence, water saturation can be found with the help of a number of CT images for different test conditions. $CT_{wet}(T)$, $CT_{dry}(T)$ are the CT values of the core sample when it is completely saturated by water and when the sample is completely dry, respectively. Their difference gives the relative spatial distribution of water in the 100% water saturation case. At a test condition, there will be a mixture of water and steam within the core. Hence, the difference between $CT_{exp}(T)$ and $CT_{dry}(T)$ gives a relative measure of water distribution within the core. Hence, from Eq. 1.1 one can find the water saturation.

$$S_w = \frac{CT_{\exp}(T) - CT_{dry}(T)}{CT_{wet}(T) - CT_{dry}(T)} \tag{1.1}$$

Similarly, the porosity of the core sample can be found using Eq. 1.2. Here, CT_{water} and CT_{air} are the CT numbers of water and air, respectively.

$$\phi = \frac{CT_{wet}(T) - CT_{dry}(T)}{CT_{water}(T) - CT_{air}(T)} \tag{1.2}$$

1.1.2 Experimental Equipment

The experimental equipment that we use brings the core to the desired temperature and pressure conditions, and injects or drains water as necessary. The schematic of the equipment is shown in Fig. 1.1; the inset shows the core holder. The core is machined and inserted in an aluminum cylinder filled with high-temperature epoxy, which is then cured at 160 °C. To control the temperature in the core, an oil bath is used. The oil with a controlled temperature is passed through an external aluminum coil around the core holder. We applied thermal insulation around the aluminum coil. Aluminum is preferred for its transparency to X-rays. For the same reason, the insulation material is put together using aluminum tapes and the core is wrapped with aluminum foil after the insulation is applied. That way, we were able to keep the temperature constant in the core.

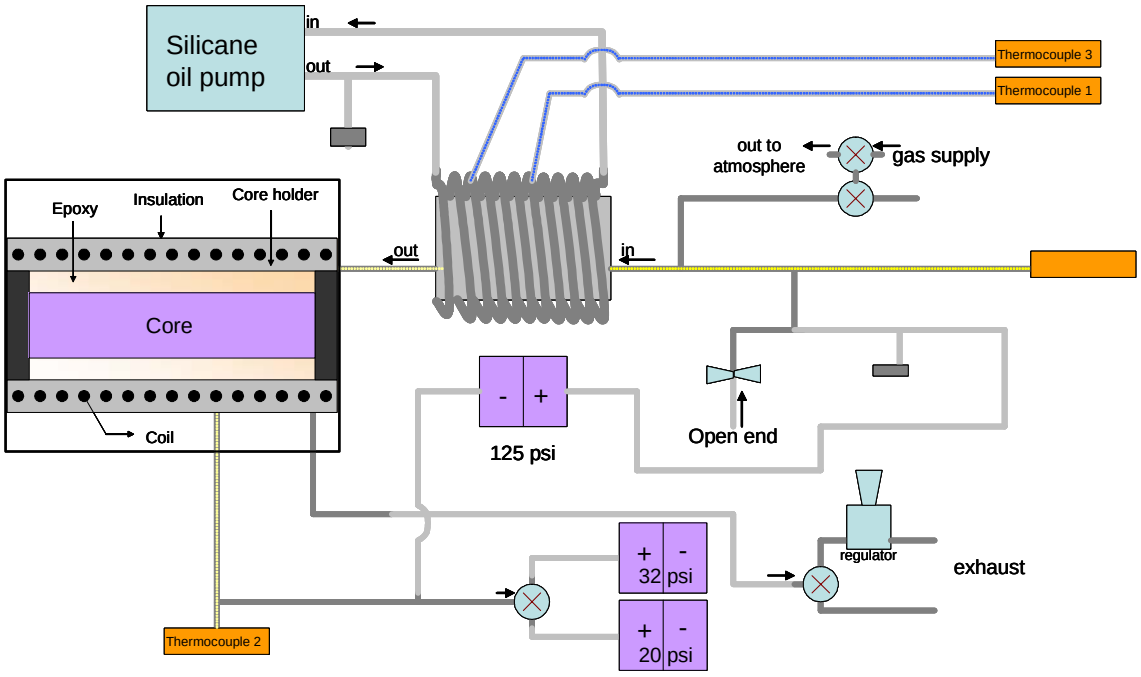

Figure 1.1: Schematic of the equipment (inset is the core holder).

In the apparatus, the vacuum pump is used to remove the air in the core sample such that a steam-water environment can be established. Water is delivered using a water pump. The amount of the water delivered and leaving the sample can be recorded in the computer using an interface.

Note that the coil and the insulating material that is wrapped over the core holder are transparent to the X-rays emitted by the CT tool to ensure a reliable measurement.

1.1.3 Measurement Procedure

Our aim is to measure the CT_{dry}, CT_{wet}, and the CT_{exp} values that are needed to calculate the S_w and ϕ parameters through Equations 1.1 and 1.2. For that, first the core holder is dried by heating it to a temperature of ~100 °C and pulling a vacuum for ~48 hours. CT measurement gives the CT_{dry} value. Next, the core is saturated with water under vacuum after the sample is cooled down to room temperature. To ensure that the sample is saturated with water completely, a pressure of 50 psi is applied. The temperature can now be elevated up to ~100 °C to get the CT_{wet} measurement. The temperature and the pressure can be varied to obtain a data set with respect to these parameters. Fig. 1.2 shows one such measurement of water saturation with respect to pressure at constant temperature that was taken by Li and Horne (2003).

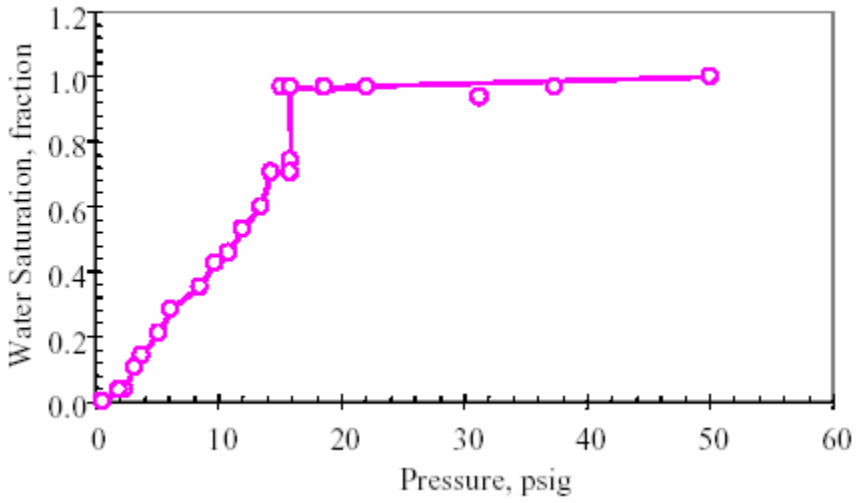

Figure 1.2: Variation of in-situ water saturation in The Geysers rock with pressure at a temperature of 120 ℃. (Horne et. al ,2003).

1.2 CURRENT STATUS

In the previous report we mentioned that leakage was a problem in the apparatus. After a systematic procedure we had determined that the leak was due to the transducers. We ordered new pressure transducers with ratings 32 psi and 125 psi. They were installed as seen in Fig. 1.1 and their calibration was completed.

With the new equipment, we performed pressure drop tests to measure the relative permeability value of the rock. For that we used the pressure pulse decay method. This method uses only the pressure data to infer the relative permeability. We did not have a very reliable tool to measure the flow rate. In Section 1.2.1 we explain how these measurements can be used to calculate the permeability.

We will use the CT tool to measure the in-situ saturation and porosity of the sample. During this quarter, we focused mostly on calibrating the system and made some preliminary measurements. X-ray beam-hardening effects and other problems prevented us from obtaining reasonable CT values. However we were able to gain experience with the system.

1.2.1 Permeability Tests

Steady-state measurement of very low permeability is limited by the need to measure very small flow rates. In the literature, the pressure-pulse decay method was introduced (Persoff, 1996) to eliminate the need to measure the flow rate. In the unsteady pressure-pulse-decay method, reservoirs up-and downstream of the sample are initially at different pressures, and the pressures in the up- and downstream reservoirs respectively fall and rise as fluid flows through the sample. One can infer the flow rate from the changes in pressure

rather than by measuring it. The analytical solution of this technique was derived by Ning (1993). For this technique to be viable, the upstream and downstream reservoirs must be small. In our equipment most of the reservoir volume is contained in the valves and transducers, and hence the technique is expected to yield reasonable results. We measured the downstream pressure and the differential pressure as a function of time. Fig. 1.3 shows the pulses we generated and their decay as a function of time.

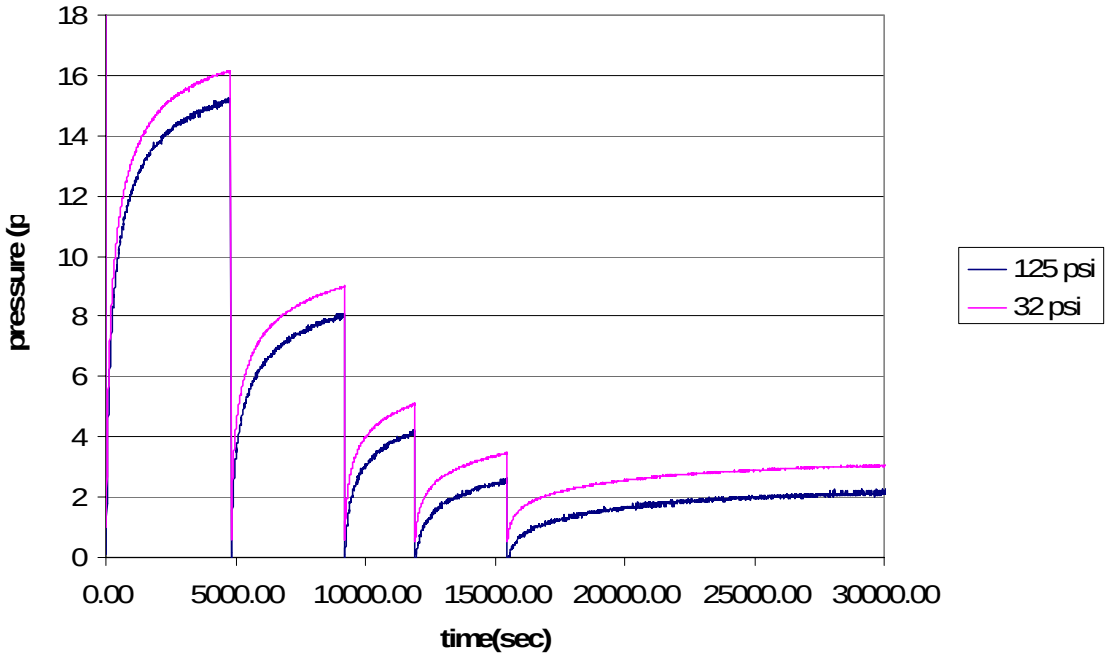

Figure 1.3:Pressure pulses as a function of time

Persoff (1996) used a less rigorous interpretation of the pressure pulse decay data. In that paper, the compressibility of the gas and the storage capacity of the sample were ignored. That way, the problem was reduced to a simple falling-head permeability test. In such a test, the differential pressure between the two reservoirs decays exponentially with time. Persoff (1996) calculated the permeability as a function of pressure difference:

$$k = (VM\mu L \ln'(\Delta p))/(2RT\rho A) \qquad (1.3)$$

where k is the permeability, M and μ are the molecular weight and the viscosity of the gas, L and A are the sample length and cross sectional area, ρ is the density at the average pressure.

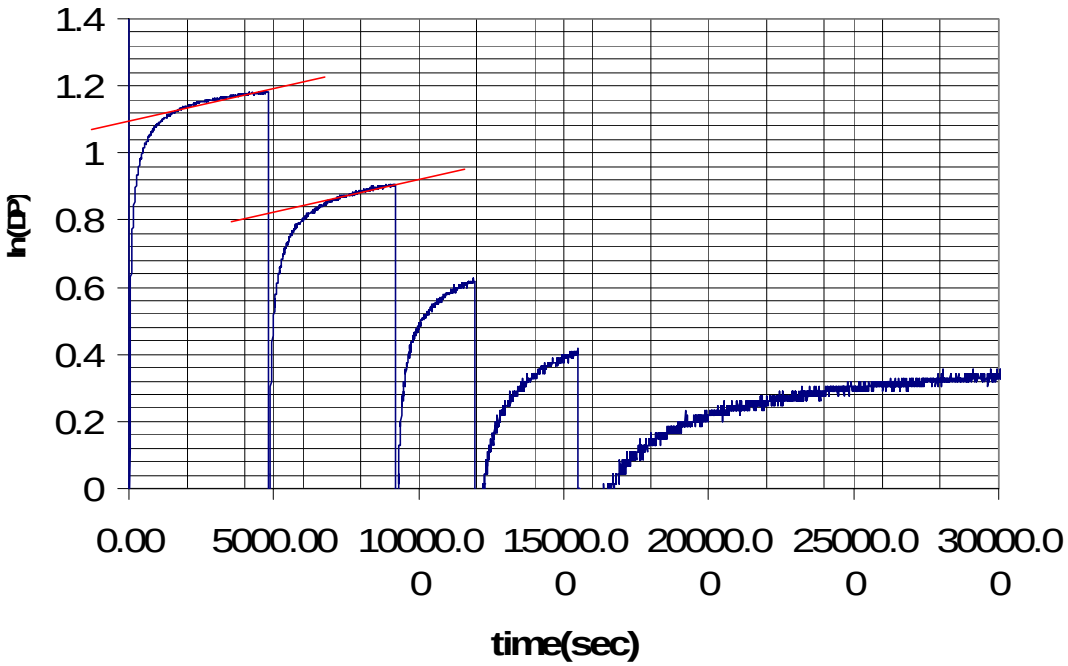

Figure 1.4: Natural logarithm of the pressure difference as a function of time.

The values for our system are (nitrogen is used as the fluid):

$\mu = 1.779\times10^{-5}$ kg/m-s = 0.0178 cp
L = 8.89 cm
A = 57.5 cm^2
$\rho = 1.25$ kg/m^3
R = 8.3145 J.mol K°
T = 300 K°
M = 14 g/mol

We need to find estimates for input and output reservoir volumes. Since it is only the tubing and the measurement apparatus; for an order of magnitude calculation we can take V=50 cm^3. Also from Figure 1.4, $\ln'(\Delta p)=2\times10^{-5}$. Δp is in psi in the given data, we need to convert it to Pa for the formula.

Using these values we can find an estimate for the permeability of the system to nitrogen:

$k = 1.22\times10^{-17}$ m^2 = 0.0122 md.

1.2.2 CT Measurements

Currently, the core holder holds a sample of The Geysers rock, which was characterized previously by Horne, Reyes and Li (2003). We made the measurements using a Picker™ Synerview X-ray CT scanner (Model 1200 SX). The sample holder is placed within the gantry, which is a large ring as seen in Fig. 1.2, which contains the X-ray tube and the X-ray detectors. During a CT scan the X-ray tube makes a complete rotation around the core. The x-ray beam is collimated to the slice of the sample being imaged. At any instant of

time during the scan, this beam of X-rays is attenuated by the sample. Different parts of the beam are attenuated by varying amounts, depending on the types and amounts of material the X-rays pass through. Water-saturated rock attenuates the X-ray beam differently than unsaturated rock. Once the X-ray beams pass through the sample and are attenuated, their remaining intensity is measured by an arc of about 500 X-ray detectors. These X-ray measurements by the detectors are repeated at different angles during the scan. The X-ray detectors produce electronic pulses proportional to the X-ray intensity they receive. These hundreds of thousands of data pulses, from different detectors and at different positions of the X-ray tube, are fed into a computer which uses them to form a digital image of the slice of the sample through which the X-rays passed. In creating the image, the computer assigns each pixel a value, called the CT number. The larger the CT number the greater the attenuation of the tissue represented within that pixel and the brighter that pixel will appear in the image. By definition, air has a CT number of negative 1000 and water has a CT number of zero. Therefore it is possible to deduce how much the sample is saturated and measure the saturation as a function of other variables.

As explained in Section 1.1.1, we would like to measure $CT_{wet}(T)$, $CT_{dry}(T)$, and $CT_{exp}(T)$ values. Fig. 1.5 shows the experimental equipment placed in the CT scanner.

Figure 1.5: Equipment placed in the CT scanner.

We first heated the sample using the oil bath to a temperature of 100 °C for two days. We monitored the temperature using the thermocouples. The temperature within the core was about 60 °C. The temperature in the aluminum coil was 80 °C. This showed that there is significant heat loss while oil is circulated and we need to improve the insulation of the system. However, the temperature stayed constant during the test. After the sample was

heated a vacuum was applied to remove the air inside the core. That way the core was completely dry. The CT measurement at this stage gave us the CT_{dry} value.

Then we removed the vacuum to start the saturation at room temperature. A water beaker was connected to the inlet of the system. The water beaker was on a balance. We monitored the system until the influx stopped, i.e., until the balance reading remained constant. Then for further injection, we used a water pump until we saw water coming from the outlet. The core inlet pressure was kept at 50 psi during this stage. The system was fully saturated at the end of this stage. We took another CT measurement at this point, to give us the CT_{wet} value.

Both of these measurements were taken at room temperature. We then increased the temperature to 50 °C inside the core. Our aim was to see the effect of temperature on the CT value. An unfortunate power black-out during the test caused the CT scanner to reset. As a consequence, the equipment was pushed backwards from the gantry, damaging the pipe and valve connections, and breaking the beaker used for water injection. The CT measurements need to be taken without changing the location of the sample. Therefore we had to check the calibration, check for leaks and start all over again for the CT measurements.

1.3 CONCLUSIONS

At this stage, we have analyzed the experimental equipment component by component and made the necessary adjustments to ensure robustness. All the components, including the CT scanner, are now available to use. Due to the unfortunate power black-out incident we had to restart the calibration from the beginning. From now on, saturation and porosity values can be measured. In this report we also discussed about a method to measure the permeability of rock to nitrogen. The technique we used, the pressure-pulse decay method, eliminates the need to measure flow rate, which is often difficult. However it will be interesting to compare the results of the pressure-pulse decay test with the usual way of pressure/flow rate measurement.

At the moment, the core holder holds a sample of Geysers rock. After the characterization of the Geysers rock, we will compare our new results with those of the previous characterization. Then we are planning to begin the analysis of new rock samples.

2. DOWNHOLE ENTHALPY MEASUREMENT

This research project is being conducted by Research Assistant Egill Juliusson, Senior Research Engineer Kewen Li and Professor Roland Horne. The objective of this project is to investigate ways to measure enthalpy downhole either by constructing a device specifically for that purpose or by expanding the use of existing measurement technologies.

2.1 SUMMARY

The experiment described in the previous Quarterly Report was extended to include more sensors and a flow meter. The circuits for the sensors were also rebuilt and modified in order to produce a better signal. Three separate tests, with variable air and water flow rates, were run.

A clear change was seen in the signal when a bubble passed both the resistivity and the phototransistor sensors. The thermocouple measurement did not show a similar response. Additionally, a relatively clear pattern, which would enable a good estimate of the air- and water flow rates, was seen in the signal when the flow rates were small. For larger flow rates the pattern became unclear and it is yet to be determined if that signal can be used to infer the flow rates accurately.

Future work includes establishing more reliable methods for interpreting the time shift and flow rate ratios from the measured signals and working on downhole application design. Looking at other methods for determining the enthalpy will also be considered, e.g. trying to infer enthalpy from the vertical pressure gradient or a combination of known well logs and/or well testing methods.

2.2 PILOT TEST

2.2.1 Reconfigured experiment setup

The pilot test described in the previous Quarterly Report was reconfigured to include more sensors, more efficient circuitry and a simple flow meter. A schematic diagram of the experiment is shown in Figure 2.1. The figure shows how a mixed air/water flow (flowing vertically upwards) passes three types of sensors, at three different locations. At locations 1 and 2 we have a phototransistor, temperature and resistivity measurement. At spot 3 we only have a temperature measurement. After the fluid mixture has passed the sensors it is separated and the quantity of each fluid component is measured over a specific time interval to find each individual flow rate.

The circuitry for the phototransistor and resistivity sensors, shown in Figure 2.2, was also improved and somewhat simplified. Some of the more important improvements were, using a shielded, shorter cable and a common, stable voltage source and reconfiguring the circuit so that it measured the voltage drop over a reference resistor. Some other adjustments were made to reduce the noise in the temperature measurement, e.g. grounding the terminal block and wrapping the thermocouple wire in aluminum foil, but this did not

seem to have much effect. It should be mentioned that the ground connection for the terminal block may have been ineffective and should be reevaluated.

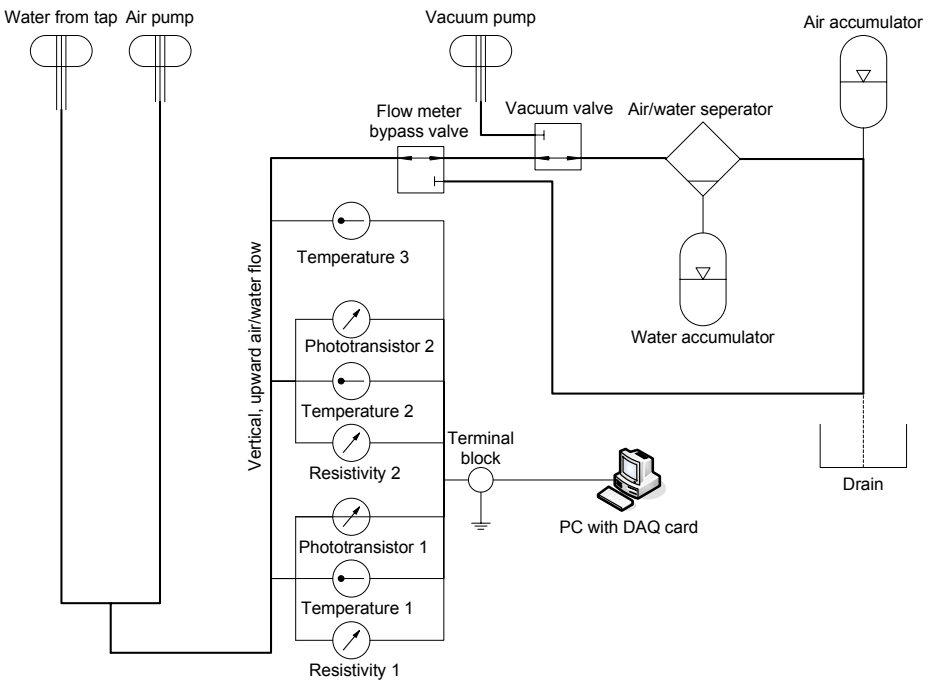

Figure 2.1: A schematic of the experiment as it was in May and June 2005. The main difference between this setup and the previous one (from March 2005) is that there are more sensors measuring the flow and the sensor circuitry has been improved. Moreover, a simple flow meter has been added.

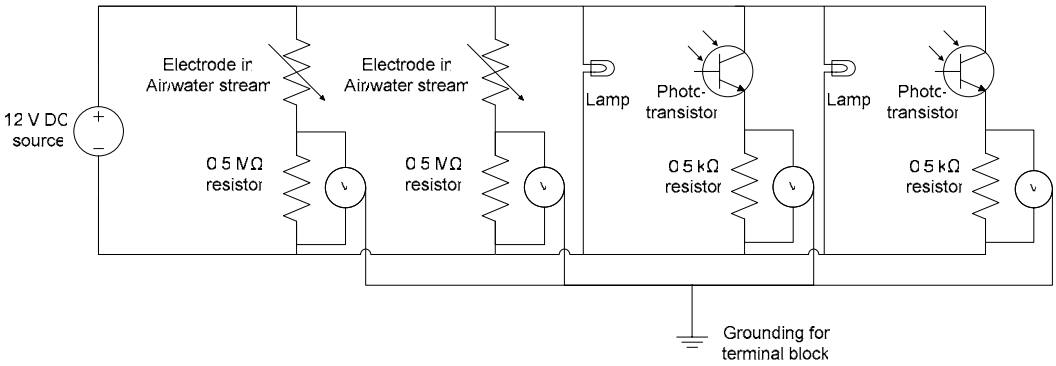

Figure 2.2: A circuit diagram for the phototransistor and resistivity sensors as it was in May and June 2005. As the diagram shows, a single 12V DC source drives the whole circuit. When an air bubble passes one of the sensors, the resistance of the electrode/phototransistor changes, hence we measure a different voltage drop across the reference resistor connected to the terminal block.

2.2.2 Results

Data were collected from the experiment described in Section 2.2.1. Three separate tests were run, each with different air and water flow rates. The gathered data were interpreted

to some extent, but more established methods of data analysis are preferable, e.g. for quantification of the time shift and the air/water ratio (analog to steam quality).

One goal of this experiment was to look for an identifiable signal in the temperature measurement as a bubble passes. To achieve this, a thermocouple, an electrode and a phototransistor were placed in the same location and data were collected from all three simultaneously. This way the phototransistor and electrode provided reference data to be compared to the thermocouple output. Data from a one second interval are illustrated in Figure 2.3. When a bubble passes the sensors, a clear voltage drop is seen in both the resistivity and phototransistor output but there is no clearly identifiable signal in the temperature measurement. This does not mean that the temperature data is entirely irrelevant, but alternative data is required to provide enough information to determine the steam fraction and the enthalpy.

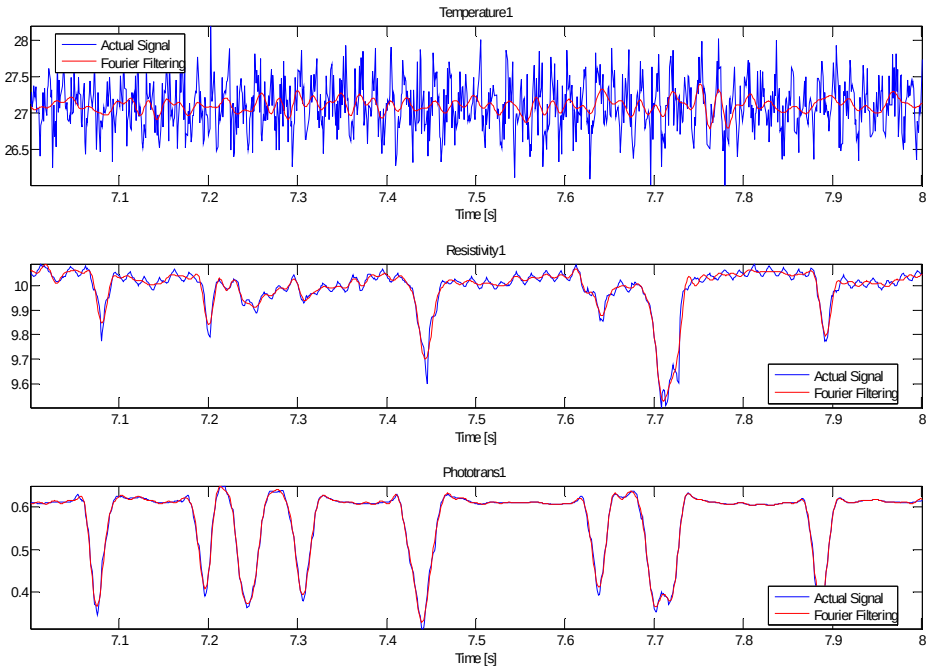

Figure 2.3: Results from Pilot Test 1, location 1. A clear voltage drop is seen in both the phototransistor and resistivity measurement, as a bubble passes. The thermocouple does not show a similar response.

A second thing to look at in this experiment is the quality of the resistivity measurement compared to the phototransistor measurement. Figure 2.4 shows plots of data collected from locations 1 and 2. The differences in the responses of the two sensor types are twofold. Firstly, there is more noise in the resistivity measurement, that mainly emanates from surrounding electrical devices (60Hz). This may be because the current through the resistivity circuit is very small (~0.01mA), hence, the contribution from induced 60Hz AC is more apparent in the signal. Secondly, we see some crosstalk between the electrodes. This means, for example, that sometimes when a bubble passes the electrode at location 1, a signal change is seen in the resistivity measurement at location 2 also. This is very clear

e.g. in the signal seen around time 7.7s in Figure 2.4. In an attempt to explain this behavior one could propose that the anode of electrode 1 and the cathode of electrode 2 are connected through the water and form another electrode. If we denote the resistance across this electrode by R_{e12} then the measured voltage drop in circuit 2 can be calculated as:

$$V_{R2} = V - I\left(\frac{1}{R_{e2}} + \frac{1}{R_{e12}}\right)^{-1} \quad [\mathrm{V}] \tag{2.1}$$

where R_{e2} is the voltage drop across electrode 2, V = 12V is the total voltage supplied to the circuit. When a bubble passes electrode 1 the connection between electrodes 1 and 2 weakens and R_{e12} goes up. From Equation 2.1 we see that this leads to a lower value of V_{R2}. The change in the signal because of this disturbance is much smaller that the change in the signal if the bubble were passing at location 2 because $R_{e12} >> R_{e2}$.
A similar relation should exist the other way around, between electrodes 2 and 1, but it is perhaps not seen as strongly because the current can not travel as easily upstream, i.e. R_{e12} is not equal to R_{e21}. This might for example be because of a second bubble, traveling in between the sensors, that impedes the current.

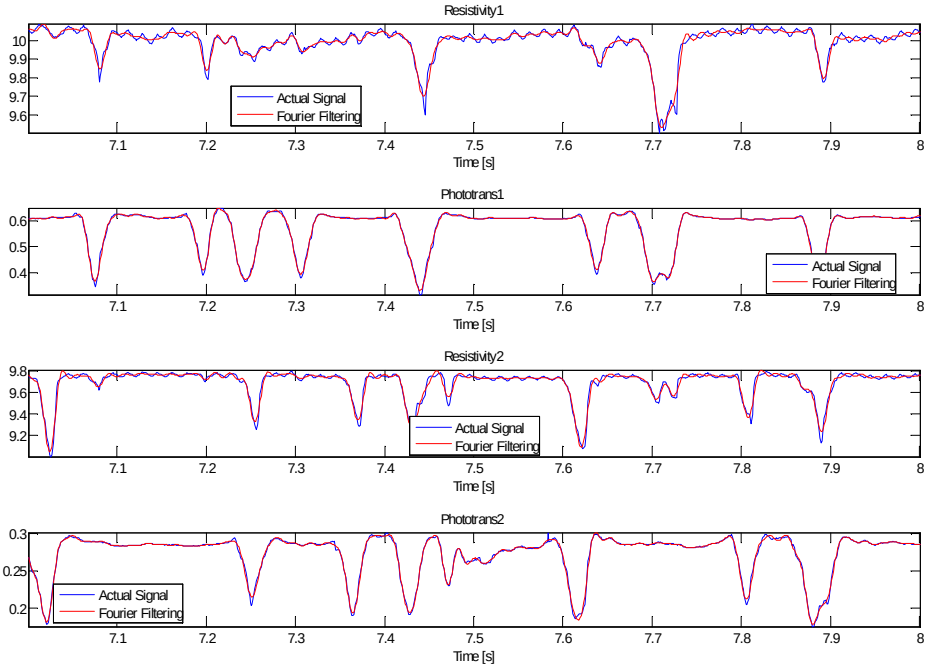

Figure 2.4: Results from Pilot Test 1, locations 1 and 2. A comparison between the resistivity and phototransistor measurements shows that the resistivity measurement is more susceptible to noise from surrounding electrical equipment and crosstalk between circuits.

It should be pointed out that in Figure 2.4 a clear pattern can be seen between the signals measured in each spot (especially in the phototransistor signal). From this pattern the time shift can be roughly quantified as 0.18s. A more robust and reliable method to determine the time shift is yet to be established.

As mentioned earlier, three separate experiments were run, each with different air and water flow rates. The flow rates for Pilot Tests 1, 2 and 3 were as shown in Table 2.1.

Table 2.1: Flow rates and flow rate ratios for air and water as measured for Pilot Test 1, 2 and 3. Calculated uncertainties are also shown for each quantity. Note that this simple flow meter has poor accuracy for low flow rates of air.

	Qair	dQair	Qwater	dQwater	Qair/Qtot	d(Qair/Qtot)	Qwat/Qtot	d(Qwat/Qtot)
Pilot Test 1	1.15	0.61 (53%)	7.43	0.37 (5%)	0.13	0.09 (64%)	0.87	0.14 (16%)
Pilot Test 2	1.41	0.32 (23%)	4.88	0.24 (5%)	0.22	0.07 (32%)	0.78	0.11 (14%)
Pilot Test 3	12.58	0.73 (6%)	4.88	0.24 (5%)	0.72	0.08 (11%)	0.28	0.03 (11%)

In Figures 2.5 and 2.6 we see the resistivity and phototransistor measurements for Pilot Tests 2 and 3. In Pilot Test 2 the air flow rate was relatively low and therefore the bubble pattern is very clear. Note again the crosstalk between the resistivity measurements at times around 1.15s and 1.30s.

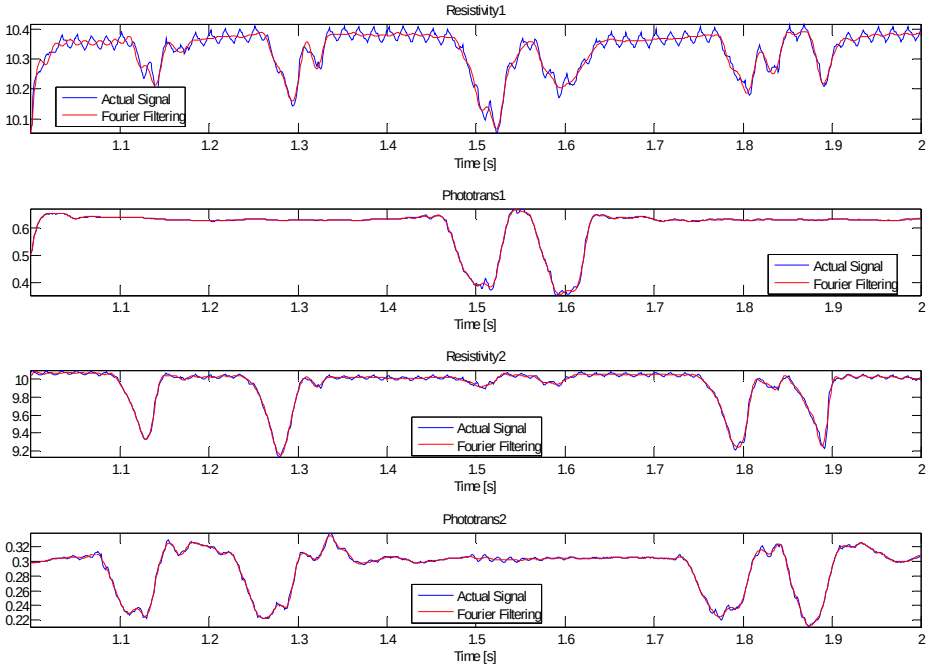

Figure 2.5: Results from Pilot Test 2, locations 1 and 2. A very clear correlation exists between the measurements taken in each spot. This enables a good estimate of the time shift and air- and water flow ratios.

In Pilot Test 3 the air flow rate was relatively high. Figure 2.6 shows the measured responses, which were now much noisier and any bubble patterns very hard to discern.
A simple way to estimate the water flow rate ratio (Q_{wat}/Q_{tot}) is to calculate the area between the measured signal at each point and the lowest measured value (shaded area in Figure 2.7) and divide that by the area between the lowest measured value and the highest measured value (area between the two red lines).

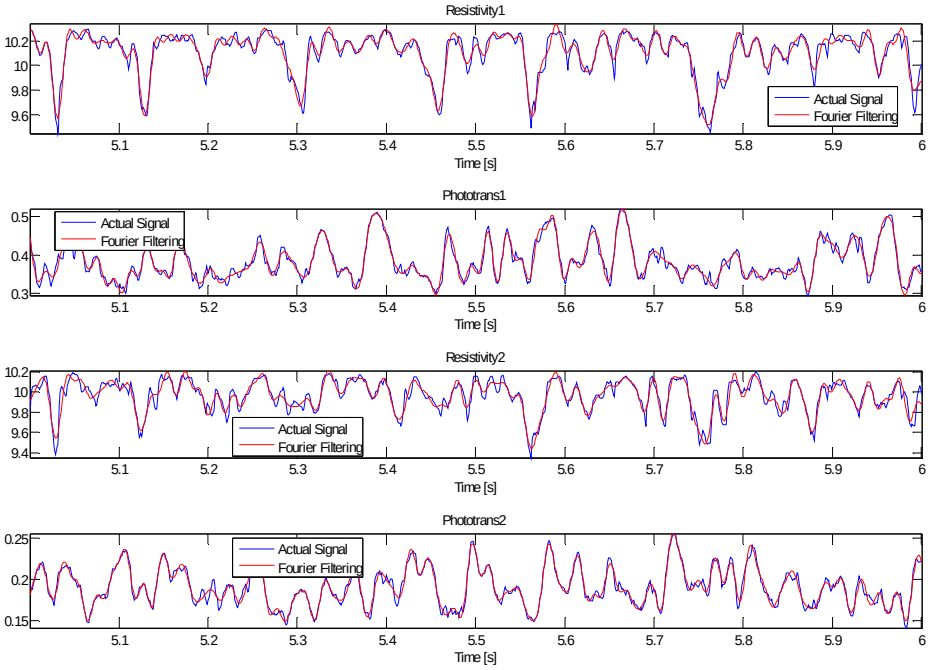

Figure 2.6: Results from Pilot Test 3, locations 1 and 2. A correlation between the measurements taken in each location is not easily detected. This is because of the high air flow rate. However, a statistical analysis of the signals might produce a reliable correlation for an estimate of the time shift and the flow rate ratios.

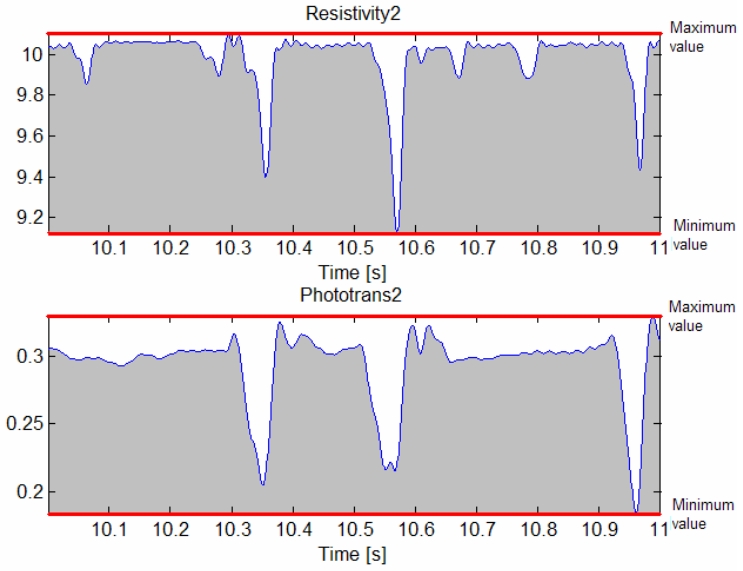

Figure 2.7: A simple method for estimating the air-water flow ratio from the signal measured. The ratio between the shaded area and the area between the two red lines should roughly equal the ratio between the water flow rate and the total flow rate (Q_{wat}/Q_{tot}).

Table 2.2 shows values obtained by this method and a comparison to the values measured with the flow meter for Pilot Tests 1, 2 and 3.

Table 2.2: The results for the method described in Figure 2.7 and the absolute deviation between these calculated values and the values measured with the flow meter.

		Resistivity 1	Resistivity 2	Phototrans 1	Phototrans 2
Pilot Test 1	Qwat/Qtot	0.88	0.88	0.74	0.73
	Abs. dev. from measured value	0.02	0.01	0.13	0.13
Pilot Test 2	Qwat/Qtot	0.92	0.90	0.77	0.70
	Abs. dev. from measured value	0.14	0.12	0.00	0.08
Pilot Test 3	Qwat/Qtot	0.84	0.74	0.44	0.42
	Abs. dev. from measured value	0.56	0.46	0.16	0.15

Comparing values from Tables 2.1 and 2.2 shows that the value inferred from the signal is within the uncertainty limit (0.14) of the value measured with the flow meter, in all cases for Pilot Test 1. In Pilot Test 2, the phototransistor values are within the uncertainty limit (0.11), but the resistivity values are slightly outside of the limit. For Pilot Test 3, all of the values are outside of the uncertainty limit (0.03).

2.3 FUTURE WORK

2.3.1 Time shift and flow rate ratio

The method illustrated in Figure 2.7 to find the water flow rate ratio is convenient in the sense that is simple and quickly formulated. However, a more efficient and reliable method, which works for all cases, is needed. Inferring the time shift and flow rate ratios from a signal like the one in Pilot Test 3 will clearly be a challenging task. Hopefully, that process can be made easier using statistical methods to find a unique correlation between the signal and the measured flow rates. It is quite likely that methods established in seismology can be helpful in determining the time shift, because finding the time between two corresponding peaks in a signal is what is what needs to be done when locating the epicenter of an earthquake with a seismograph.

2.3.2 Full size application design

The pilot tests run until now have all been in 1/8 in. tubes with segmented air/water flow. It will soon be time to move over to a larger pipe (4 in.) and start experimenting with various sensor designs. Initially the goal is to design a sensor or sensor housing that is sturdy but which does not disturb the flow too much and which enables accurate detection of the passing bubbles. At a later stage, issues concerning downhole applications need to be considered, e.g. heat, pressure and corrosion resistance.

2.3.3 Other methods

Some time might be spent on looking at alternative methods for deriving the enthalpy. One idea is to try to infer the enthalpy from the vertical pressure gradient, *dp/dz*, acquired from a standard well pressure log. As the fluid flashes in the well bore, the pressure gradient becomes smaller. Although many other physical processes affect the pressure gradient as the fluid flashes, a theoretical model could be useful, either for backing out the enthalpy or just to clarify the significant factors involved.

A second option is to try applying the pressure pulse method, which is well known in the oil industry, to meter the gas and oil rates in wells. The method uses the water hammer effect and the Darcy-Weisbach equation to infer the mixture velocity and the void fraction.

Finally, a method for utilizing logs from multiple variables to determine the value of an additional dependent variable might be of use. The method is currently being developed by Nomura (2005) for utilization in the oil field, but it might also be of value for enthalpy determination in geothermal wells.

2.4 CONCLUSION

Some advances were made in building a pilot test experiment to evaluate potential sensor technologies useful for enthalpy measurement. A more reliable method is needed for interpretation of the measured signal. Established methods for determination of the time shift can probably be borrowed from seismology. The flow rate ratios can probably be better estimated using statistical methods, but ultimately a more precise signal and a more accurate reference flow meter are needed to obtain a sensible estimate of how well the proposed methods are performing. Future work could also include full size application design and an investigation of alternative methods, mostly derived from a more theoretical standpoint.

3. STEAM-WATER RELATIVE PERMEABILITIES IN THE GEYSERS GEOTHERMAL FIELD

This project has being conducted by Research Assistant Chih-Ying Chen, previous MS student Jericho Reyes and Prof. Roland Horne. The goal of this research was to infer field-scale steam-water relative permeabilities from actual production data provided by DOGGR database. Through this study, actual production data from one active geothermal field in California, The Geysers, were used to calculate the relative permeabilities of steam and water. The estimated values of relative permeability in The Geysers geothermal field lie between the X model and the Corey model and conform mostly to the viscous-coupling model. To resolve the issues of obtaining more representative in-place water saturation, we developed the viscous-coupling correlation which leads the k_r versus S_w curves from field data to a more conventional appearance. After further denormalizing water saturations using reported minimum and maximum residual water saturations, the possible lower and upper bounds of relative permeabilities in The Geysers geothermal field were suggested. The lower bound result shows good agreement with our laboratory investigation results of rough-walled fractures. This provides better understanding of the fluid flow interactions in actual geothermal reservoirs.

3.1 BACKGROUND

As is well known in earth sciences, the outcome of any physical interaction among wetting fluid, nonwetting fluid and rock in geologically complex fractured media depends highly on the length scales studied. Therefore, knowledge of the field-scale relative permeabilities of steam and water provide more direct and accurate information in estimating the performance of a geothermal field and its capacity for further exploitation. Simulations of multiphase flow in fractured geothermal reservoirs required knowledge of relative permeability functions. In spite of considerable theoretical and experimental efforts during the last two decades for all of these issues, neither general models describe relative permeabilities satisfying, nor direct and agreeable methods calculated field-scale relative permeabilities in actual geothermal reservoirs.

In studies of fracture flow and pipe flow models, the earliest fracture model proposed was the X model ($k_{rw}=S_w$, $k_{rg}=S_g$), which assumed no phase interference between the two phases. However, many studies confirmed that this ideal situation seemed impossible to achieve in real fractures (Chen et al., 2004; Fourar et al., 1993). Subsequently, some fracture models were suggested based on representing the flows in fractures as flows in porous media or two ideal parallel planes.

In porous media, the Corey model has been widely used for modeling two-phase relative permeability (Corey, 1986). The Corey relative permeability functions are given as:

$$k_{rw} = (S_w^*)^4 \tag{3.1}$$

$$k_{rg} = (1 - S_w^*)^2 [1 - (S_w^*)^2] \tag{3.2}$$

In these equations, S_w^* is the normalized water saturation defined by:

$$S_w^* = \frac{S_w - S_{wr}}{1 - S_{wr} - S_{gr}} \tag{3.3}$$

where subscript *r* refers to residual saturation. The Corey model represents strong phase-interference in comparison to the X-model (see Figure 3.1).

In the model of ideal parallel planes, Fourar and Lenormand (1998) assumed that the complexity of the real flow in the fracture can be modeled, to a first approximation, by viscous coupling between the fluids, which is derived by integrating Stokes' equation for each stratum. Identification of the established equations and the generalized Darcy equations leads to the so-called viscous-coupling model:

$$k_{rw} = \frac{S_w^2}{2}(3 - S_w) \tag{3.4}$$

$$k_{rg} = (1 - S_w)^3 + \frac{3}{2}\mu_r S_w (1 - S_w)(2 - S_w) \tag{3.5}$$

where $\mu_r = \mu_g/\mu_w$ is the viscosity ratio. These equations show that the relative permeability of the nonwetting fluid depends on the viscosity ratio μ_r.

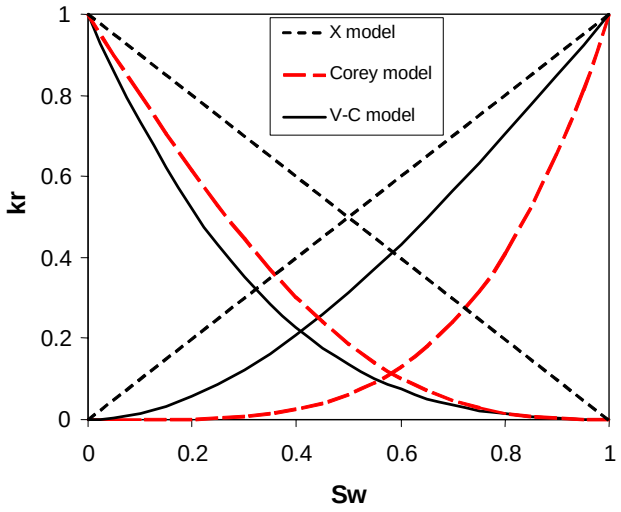

Figure 3.1: Comparison of relative permeability curves from X model, Corey model and viscous coupling model. (No residual water saturations were used in the Corey model)

There have been numerous attempts to characterize the steam and water relative permeability curves both experimentally and theoretically. The main difficulty of direct measurement has been the phase changes that occur during steam and water multiphase flow. On-going research on steam-water relative permeability in fractures gives us some insight on the characteristics of the interaction of these two phases. In the previous report (also in Chen, 2005), we developed a method to compare steam- and air-water transport through single fractures. The main finding was that steam-water flow behavior in fractures is different from air-water flow. Despite the achievements in these laboratory-scale studies, considerably limited studies have been done in developing field-scale steam-water relative permeabilities in actual geothermal reservoirs. Based on an earlier work due to Grant (1977), Shinohara (1978) described a method to estimate the steam and water relative permeabilities in geothermal reservoirs using field data. The laboratory-scale production data, saturations and relative permeabilities have verified this method as described in Reyes et al. (2004). In this study, we apply this method to The Geysers geothermal field, which is a vapor-dominated reservoir field located in Northern California about 130 km north of San Francisco. The data of The Geysers field were obtained from the DOGGR database, which has been made available publicly by the California Division of Oil, Gas and Geothermal Resources.

3.2 METHODOLOGY

Shinohara (1978) described a method to estimate the steam and water relative permeabilities in geothermal reservoirs based only on the production flow rate history and the temperature of the reservoir. To apply this method, the following assumptions have to be approximately satisfied:

1. The pressure gradient is constant for a reasonable time in each well.
2. The product of permeability and flowing area is constant in each well.
3. Fluid flow follows Darcy's law.
4. Flow to the well is predominantly horizontal.

Under these assumptions, the steam-water flow in a geothermal reservoir follows Darcy's law:

$$Q_w = \rho_w \frac{k}{\mu_w} k_{rw} A p' \tag{3.6}$$

$$Q_s = \rho_s \frac{k}{\mu_s} k_{rs} A p' \tag{3.7}$$

where Q is the mass flow rate, ρ is the density, μ is the dynamic viscosity, k_r is the relative permeability, k is the absolute permeability of the geothermal rock, A is the cross sectional area of flow, and p' is the pressure gradient. The subscript ($_w$) and ($_s$) refer to water and steam respectively.

Dividing Equation (3.6) by Equation (3.7) gives us:

$$\frac{Q_w}{Q_s} = \frac{\upsilon_s}{\upsilon_w}\frac{k_{rw}}{k_{rs}} \tag{3.8}$$

where υ is the kinematic viscosity. Taking the sum of Equations (3.6) and (3.7) gives us:

$$Q = Q_w + Q_s = \left(\rho_w \frac{k_{rw}}{\mu_w} + \rho_s \frac{k_{rs}}{\mu_s}\right) kAp' = \left(\frac{k_{rs}}{\upsilon_s}\right)\left[1 + \left(\frac{Q_w}{Q_s}\right)\right] kAp' \tag{3.9}$$

where Q is the total of mass production rate of steam and water.

If we assume kAp' is constant in each well, then Equation (3.9) shows that a plot of Q vs Q_w/Q_s would be almost linear when Q_w/Q_s is small, and we can find the value of kAp' from either the intercept or the gradient of the line on the graph. This intercept, where $Q_w/Q_s = 0$, becomes Q^*, where:

$$Q^* = \frac{1}{\upsilon_s} kAp' \tag{3.10}$$

Because $k_{rs} = 1$ at $Q_w = 0$, then, substituting Equation (3.10) into Equations (3.6) and (3.7),

$$k_{rw} = \left(\frac{\upsilon_w}{\upsilon_s}\right)\left(\frac{Q_w}{Q^*}\right) \tag{3.11}$$

$$k_{rs} = \frac{Q_s}{Q^*} \tag{3.12}$$

Therefore knowing Q^* , we can calculate k_{rs} and k_{rw} by also knowing Q_w, Q_s, υ_s, and υ_w Unfortunately, the actual in-place water saturation cannot be inferred merely from the production data in actual geothermal reservoirs. To estimate water saturation using the production data only, the volumetric ratios can be used to infer the reservoir water saturation in the absence of residual saturation and for homogeneous flow of both phases. This estimated water saturation is called the *flowing* water saturation in geothermal engineering, and can be calculated from:

$$S_{w,f} = \frac{(1-X)\nu_w}{(1-X)\nu_w + X\nu_w} = \left(1 + \frac{1}{\mu_r}\frac{k_{rs}}{k_{rw}}\right)^{-1} \tag{3.13}$$

Hence, the relative permeability ratio can be expressed as

$$\frac{k_{rs}}{k_{rw}} = \mu_r \left(\frac{1 - S_{w,f}}{S_{w,f}} \right) \tag{3.14}$$

where X is the mass fraction of steam and v_w and v_s is the specific volume of water and steam, respectively. By definition, this flowing saturation is identical to the *fractional flow* in the previous chapters. It must be understood that the flowing saturation is different from the actual in-place (*static*) saturation in a geothermal reservoir. This also reveals the main limitation of the Shinohara method; *the field production data carry no information about in-place saturation*.

To overcome this problem, some representative correlation functions of in-place water saturation against flowing water saturation is needed. To avoid confusion, unless term "*flowing*" is used, the saturation used in this chapter denotes conventional in-place saturation (or static saturation). Note that the flowing saturation $S_{w,f}$ is equivalent to the fractional flow f_w described in the petroleum literature. In the next sections, we apply this method to field data from The Geysers geothermal field, calculate its relative permeabilities, and study possible correlation between flowing water saturations and in-place water saturations in this field to obtain more conventional and representative relative permeability curves.

3.3 RESERVOIR APPLICATIONS

The production data in The Geysers geothermal field from DOGGR include temperature, pressure, steam and water production rates. The Geysers reservoirs have well head temperature ranging from 180 to 230^{o}C. In choosing the wells to be used in this study, a number of issues had to be addressed. First, for the vapor-dominated reservoir, we had to find data from wells that had both steam and water production. Of the 503 wells made available to us from The Geysers, only 25 produced water. Nine wells were ultimately used, as these wells had a sufficient number of readings for the calculation. Also, the first assumption of Shinohara's method tells us that it is necessary to choose a time period over which we can assume a constant pressure gradient. Since production data are usually intermittent in nature and often have periodic fluctuations, we had to find data sets that had significant stable periods.

Figure 3.2 is an example of steam and water production histories from Coleman 4-5, a Geysers well. We tried to omit extreme readings from our analysis, therefore the spike seen in 1986-1987 was not chosen as part of the range. For this work, we used a data interval from mid-1987 to 1989. Figure 3.3 shows the Q vs Q_w/Q_s graphs for Coleman 5-5. The value of Q^* is inferred from the y-intercept value from the linear fit to the graph. Table 3.1 shows the Q^* inferred from all the wells used in the study.

As can be seen in Table 3.1, the Geysers' Q^* values are close to each other. This is an extension of the second assumption made by Shinohara in developing his method. Not only is *kAp'* constant in a well, wells that are near each other or belong to the same geothermal field also have similar *kAp'* values. Since the wells in a certain geothermal

field mainly have the same *k* values, and to a certain extent, *A* and *p'*, then our inferred values are consistent with each other. To evaluate the kinematic viscosities and mass production rates of the steam and water correctly, we must infer the bottomhole conditions, as these reflect the true flowing conditions of the well. We made temperature corrections based on the documented depths of the wells.

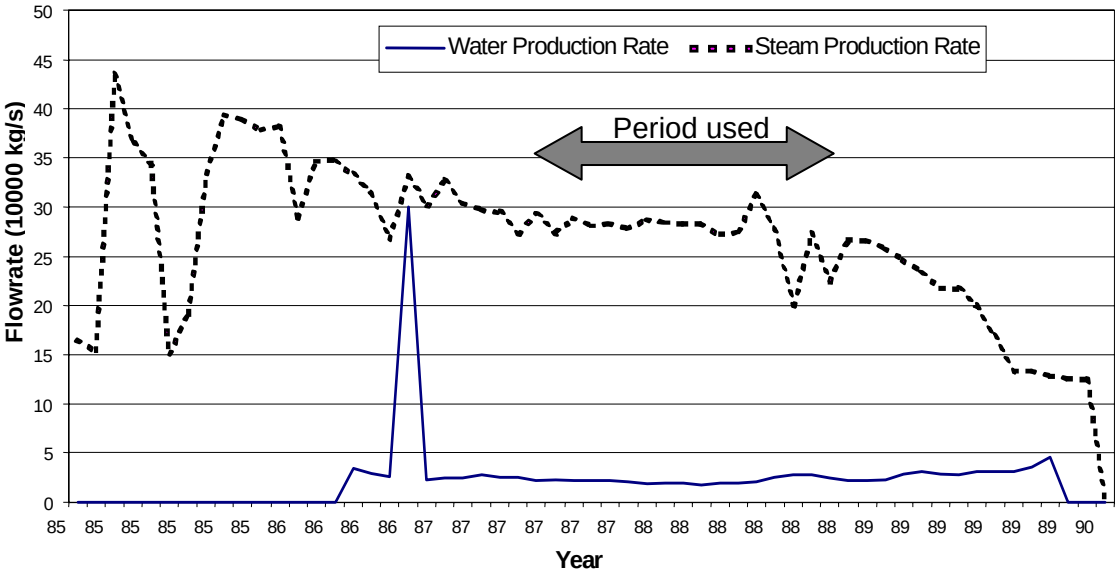

Figure 3.2: Steam and Water Production History of Coleman 4-5, The Geysers Geothermal Field.

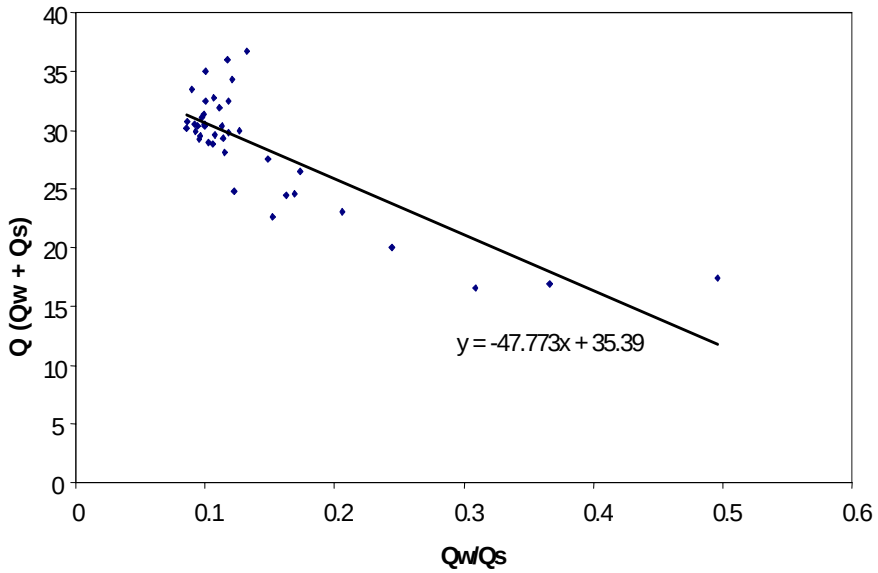

Figure 3.3: Q vs. Qw/Qs to infer Q for Coleman 4-5, The Geysers Geothermal Field.*

Table 3.1: Inferred Q values for wells from The Geysers Geothermal Field.*

Geysers Wells	Q^*
Coleman 4-5	35.39
Coleman 5-5	35.649
Coleman 3-5	24.186
Francisco 2-5	24.182
Coleman 1A-5	24.09
Thorne 6	33.59
Thorne 1	17.384
Francisco 5-5	23.52
CA-5636 6.8E-20	27.868

After these procedures, Equations (3.11) and (3.12) were used to calculate the relative permeabilities of steam and water. Figure 3.4 shows us the plot of relative permeability with water saturation for The Geysers geothermal wells. Note that these graphs are plotted against the flowing saturation, $S_{w,f}$, as defined by Equation (3.13) because the actual (in-place) water saturation was not available. The flowing saturation excludes the immobile water or steam fractions and assumes no-slip and homogeneous flow. Because The Geysers is a vapor-dominated reservoir, we expected the low water saturation values. For the relative permeability of steam, The Geysers calculation exhibits a sharp drop in k_{rs} at small values of $S_{w,f}$. The water saturation in these figures might appear to be much smaller than the traditional behavior of relative permeability curves, but this is only because of the use of flowing saturation based on Equation (3.13), rather than the true in-place saturation. Relative permeability functions without respect to in-place water saturation are not useful in reservoir simulations for performance forecasting, because most simulators assume relative permeabilities depend on in-place saturation only and curves of k_r versus S_w are the standard form to input these simulators. To this end, a likely conversion from flowing to in-place water saturations is required.

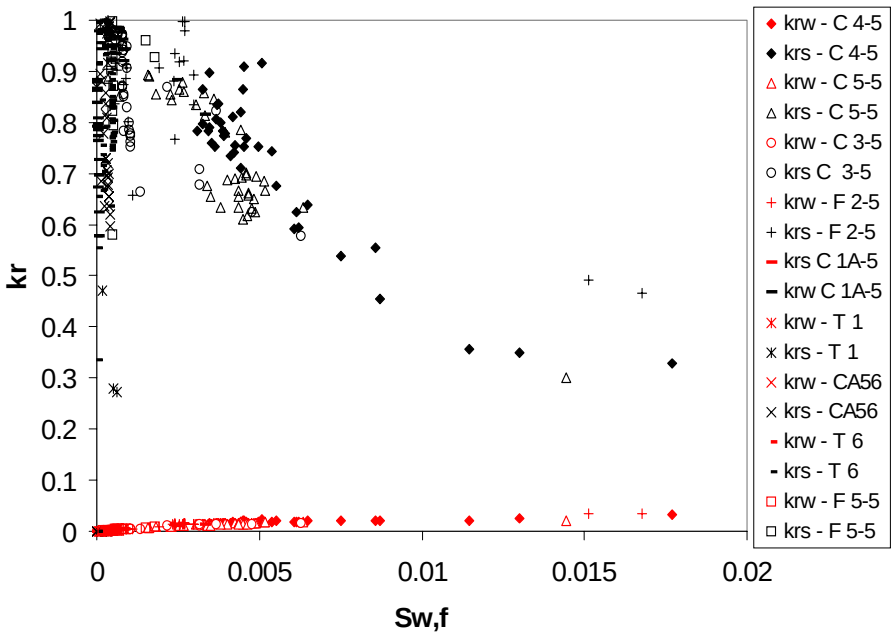

Figure 3.4: Plot of relative permeability curves against flowing water saturation for The Geysers Geothermal Field.

3.3.1 In-Place Saturation Conversion

As described, Shinohara's method seems to obtain consistent relative permeabilities for all wells considered in The Geysers field. However, the flowing saturation values inferred from Equation (3.13) are a significant underestimate of the in-place saturation. The difference between the two saturations is due to the velocity differences between steam and water phases, to the effects of immobile phases, and to the phase transformation effects. Therefore, we cannot simply use the flowing saturation to substitute for the real reservoir saturation.

The relationship between flowing and in-place water saturations was examined by comparing the actual (in-place) water saturation measured in our steam-water experiment in fractures described in the earlier quarterly reports (also in Chen, 2005) with the flowing water saturation calculated from Equation (3.13). Figure 3.5 provides possible mapping equations to relate the flowing and the actual water saturations for the laboratory scale measurements in the three fractures studied (Figure a) and theoretical outcomes from X, Corey, and viscous-coupling model (Figure b). From Figure 3.5a, the experimental results show that the flowing water saturation is significantly less than the actual water saturation. As a result, the shape of relative permeability curves was compressed leftward like Figure 3.4. The relationship between the two saturations can be expressed by logarithmic trends. The models in Figure 3.5b do not account for the residual water saturation (S_{wr}); therefore, the end-trends behave differently from the experimental results.

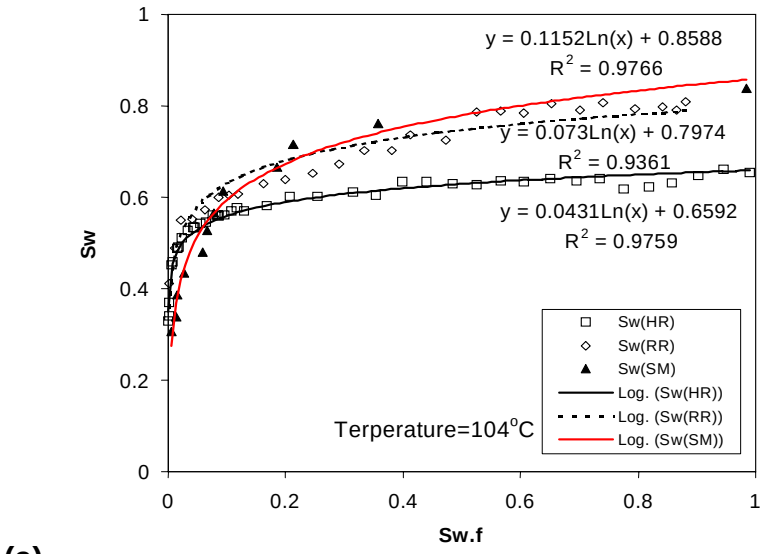

(a)

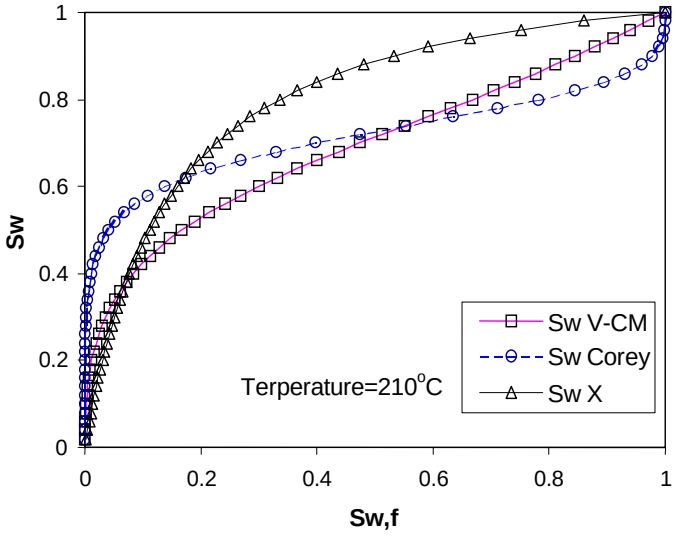

(b)

Figure 3.5: The flowing water saturation versus actual (in-place) water saturation: (a) experimental results at 104°C from Chen (2005); (b) theoretical results for reservoir conditions (210°C).

As shown in these curves, each experimental result or theoretical outcome offers a dissimilar correlation function between S_w and $S_{w,f}$. Therefore, it is crucial to choose a representative mapping equation in converting field-scale relative permeabilities. To compare the estimated relative permeability values with the experimental results as well as the three most commonly assumed models of relative permeabilities in fractures, we plotted the computed k_{rw} and k_{rs} values with these laboratory measurements and model curves in Figure 3.6. The top graph shows linear Cartesian plot, while the bottom graph

shows the logarithmic plot to demonstrate the trend of small values. We see from both graphs that the calculated values for The Geysers wells agree with the viscous-coupling model and some near-end points of the homogeneously rough-walled (HR) and randomly rough-walled (RR) fractures. Hence, the $S_{w,f}$ from field data should be similar to those calculated from viscous-coupling model since both cases have similar k_{rs}/k_{rw} in the right hand side of Equation (3.13).

Assuming that residual gas and water saturations in The Geysers field are negligible at this point, the viscous-coupling curve in Figure 3.5b is reasonable in serving as a correlation function to transform the flowing water saturation to the in-place water saturation. Substituting its relative permeability functions in Equations (3.4) and (3.5) into Equation (3.14), we obtain

$$\frac{(1-S_w)^3+\frac{3}{2}\mu_r S_w(1-S_w)(2-S_w)}{\frac{S_w^2}{2}(3-S_w)}=\frac{(1-S_{w,f})\mu_r}{S_{w,f}} \tag{3.15}$$

Since $S_{w,f}$ is known from the production data, Equation (3.15) can be written in a cubic form which was solved numerically for $S_{w,}$. After converting the (flowing) water saturation values estimated from The Geysers production data, Figure 3.7 shows the relative permeability values against the inferred (in-place) water saturation. The dashed lines are the trends for the viscous-coupling model in reservoir conditions. The relative permeabilities previously spanning from 0 to 0.23 (flowing) water saturation now range from 0 to 0.5 (in-place) water saturation after applying the viscous-coupling correlation. As expected, the relative permeability curves follows the viscous-coupling model and hence show a more conventional relative permeability behavior. Nevertheless, a steep decreasing trend from unity still can be seen from k_{rs} in The Geyser cluster, which is consistent with the laboratory investigation for HR and RR fractures.

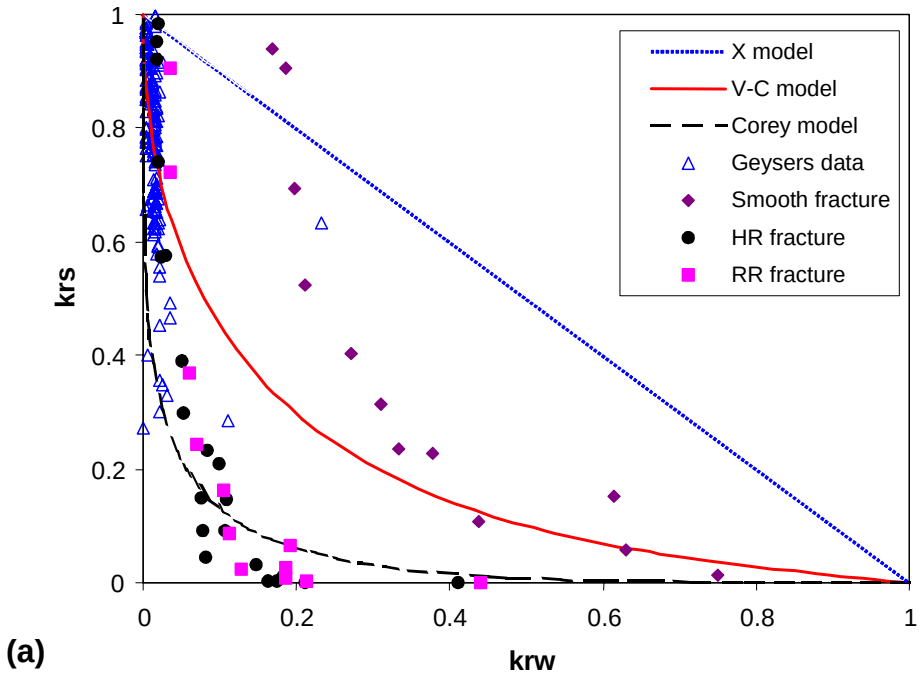

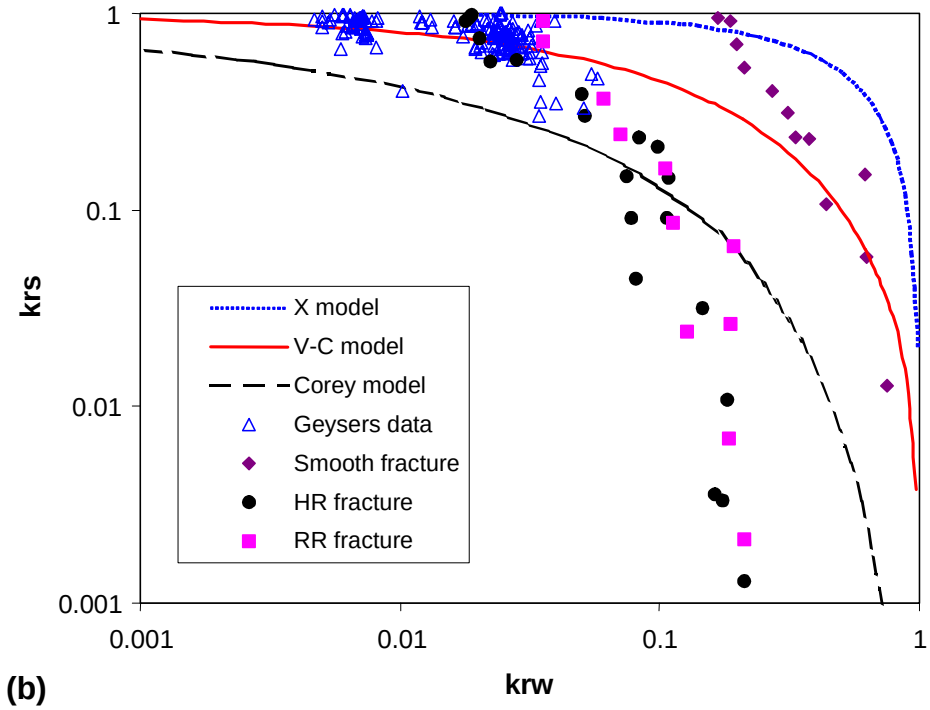

Figure 3.6: Plot of k_{rs} vs k_{rw} for The Geysers Geothermal Field, with the X, Corey, and viscous-coupling model: (a) Cartesian plot, (b) Logarithmic Plot.

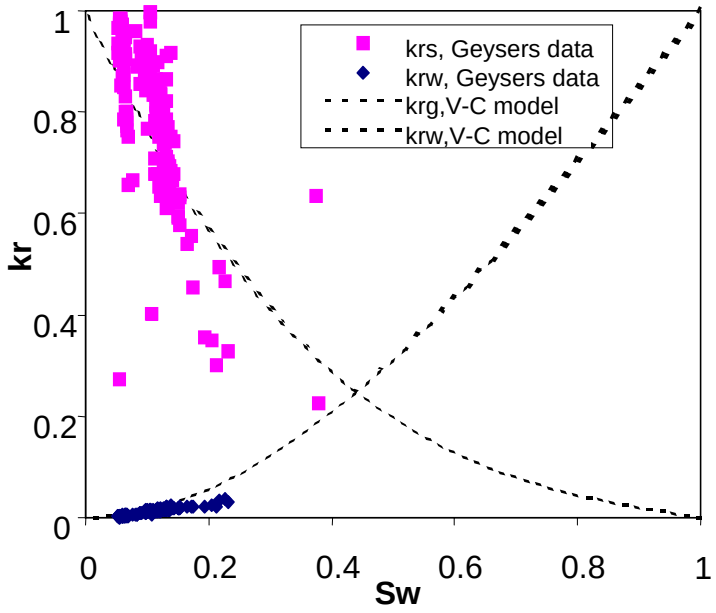

Figure 3.7: Relative permeability vs. mapped in-place water saturation from the field production data for The Geysers Geothermal field, compared to the viscous-coupling model (assuming no residual water saturation).

3.3.2 Consideration of Residual Saturation

The relative permeability cross plots in Figure 3.6 show that most Geysers data cluster lies on end points of results from the rough-walled (HR and RR) fractures though the range of k_{rw} is fairly short. Up to this moment, numerous studies have been done in The Geysers geothermal field in estimating reservoir geological and hydraulic properties (Sanyal, 1981; Belen and Horne, 2000; Reyes et al., 2003; Li and Horne, 2003; Reyes et al. 2004). Most of these studies showed that the assumption of negligible residual saturations is not practical in The Geysers field. Earlier studies have suggested some methods in estimating in-place water saturation based on production histories (Grant et al. 1982; Belen and Horne, 2000). A study applying these methods to 177 wells in The Geysers field was conducted by Reyes et al. (2003). Their results show that The Geysers field had in-place water saturation ranging from 0.3 to 0.7 during the period when production data were acquired. Since The Geysers field is a vapor-dominated reservoir, and steam mass rates are much larger than water production rates as can be seen in Figure 3.2, the in-place water saturations there may more or less approach to residual water saturation. Hence, we can consider that significant residual water saturations exist in The Geysers field. Consequently, the saturation calculated from Equation (3.15) is actually normalized water saturation, identical to Equation (3.3), rather than actual saturation. To denormalize the water saturation, information regarding residual water and steam saturations is needed. We may use the upper and lower limits to evaluate upper and lower bounds of relative permeabilities in the Geysers field, assuming reservoirs have liquid-filled initial condition ($S_{gr}=0$). In such conditions, Equation (3.3) can be written as the denormalized form:

$$S_w = S_{wr} + S_w^*(1 - S_{wr}) \tag{3.16}$$

The S_w^* were obtained from Equation (3.15). Figure 3.8a shows the lower bound relative permeability against denormalized in-place water saturation for the Geysers field using the reported minimum residual water saturation of 0.3 (Reyes et al., 2003). The relative permeabilities from HR and RR fractures in Chapter 6 also provided, because the laboratory investigation for both fractures also conform to similar residual water saturation. Good agreement was discovered between The Geysers estimates and laboratory data. Particularly, both show the steep decreasing trend from unity for steam phase relative permeabilities. This trend has been characterized as one of the unique features in steam-water relative permeabilities as discussed in Chapter 6. The upper bound behavior using the reported maximum residual water saturation of 0.7 (Reyes et al., 2003), however, reveals less conventional relative permeabilities (Figure 3.8b). The study conducted by Reyes (2003) indicates that those wells having high in-place water saturations may be influenced by the surface water reinjection.

Lastly, several issues contributing to the uncertainty of this study need to be addressed here. First, the effects of wellbore liquid hold-up and phase transformation on production rates may be significant, but are not included here. Secondly, the fracture and matrix interaction was not included in the single fracture experiments described in our previous quarterly reports. Lastly, the scale difference between laboratory and field may be important too. All these issues may outline future extensions of this subject.

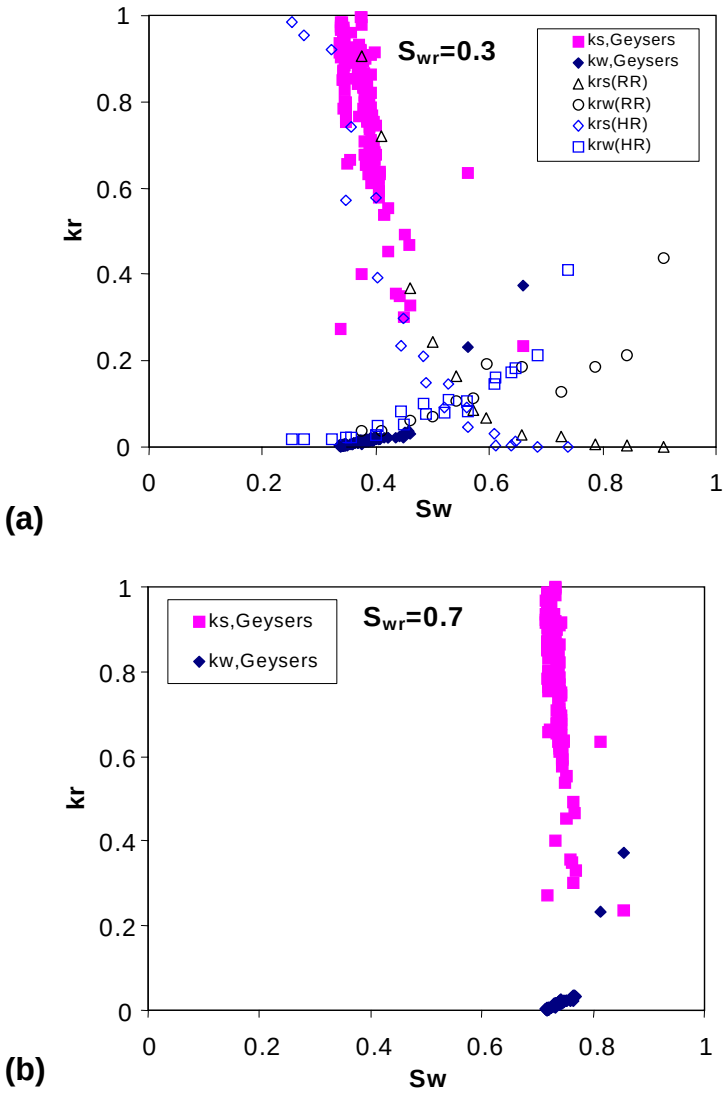

Figure 3.8: Relative permeability vs. de-normalized in-place water saturation for the Geysers field: (a) lower bound behavior using reported minimum S_{wr}=0.3, compared to the results from rough-walled fractures, (b) upper bound behavior using reported maximum S_{wr}=0.7.

3.4 CONCLUSIONS

We can infer the steam and water relative permeabilities from field measurements of the production flow rate history and bottomhole temperature. The estimated values of relative permeability in The Geysers geothermal field lie between the X model and the Corey model and conform mostly to the viscous-coupling model. By applying the viscous-coupling correlation, the k_r versus S_w curves from field data show a more conventional appearance. After further denormalizing water saturations using reported minimum and

maximum residual water saturations, the possible lower and upper bounds of relative permeabilities in The Geysers geothermal field were suggested. The lower bound result shows good agreement with our laboratory investigation results of rough-walled fractures. To estimate relative permeabilities more accurately from field production data, more representative production data as well as more accurate information about residual saturations is needed.

4. ELECTRICAL IMPEDANCE TOMOGRAPHY (*EIT*) METHOD FOR SATURATION DETERMINATION

This research project is being conducted by Research Assistant Robert Stacey, Senior Research Engineer Kewen Li and Prof. Roland Horne. The intent of this project is to develop a method to measure core saturation using electrical impedance tomography (EIT). This method is being investigated because the CT scan technique has limitations on pressures and temperatures due to the strength of the plastic core holders available.

4.1 INTRODUCTION

The idea to measure the saturation distribution in a core using EIT was described in a paper by Van Weereld, et al. (2001). The paper showed that EIT techniques were able to measure the saturation of a two-phase system (oil and brine) in near real time. Therefore this method is being investigated further in order to better understand two-phase (steam water) systems.

4.1.1 Background

The idea behind EIT is that by imposing an electric current across an inhomogeneous medium, the distribution of the internal electrical impedance will result in a variation of voltage potential at the surface. Measurements of the variable voltage potential could be used to infer the resistivity distribution within the medium. This internal distribution of electrical impedance is translated into water saturation based upon the impedance distinction between the two phases. Figure 4.1 is a diagram of a typical two-dimensional EIT experiment, consisting of 16 electrodes with an imposed current I across the core Ω, and measurement of the resulting potential V_1.

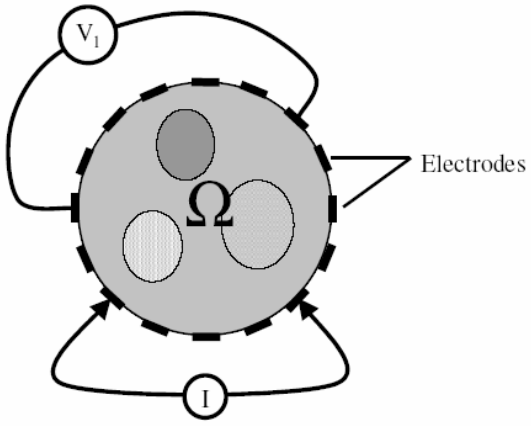

Figure 4.1: Diagram of Electrical Impedance Tomography experiment. The potential V_1 *is measured after a current* I *has been imposed across the core* Ω*. (Molinari 2003)*

The governing equation for EIT imposed upon a core Ω is:

$$\nabla \cdot (\sigma + \iota\omega\varepsilon)\nabla\phi = 0 \tag{4.1}$$

Where σ is the electric impedance of the medium, ϕ is the electric potential, ϖ is the frequency, and ε is the electric permittivity. Under conditions where low frequency or direct current is used ($\varpi \approx 0$), Equation 4.1 can be reduced to the standard governing equation for EIT (Molinari 2003):

$$\nabla \cdot (\sigma \nabla \phi) = 0 \tag{4.2}$$

The EIT inverse problem can be simplified down to a system identification problem. The cause and effect (injected current ***I*** and measured voltage ***V***) are known, but the physical system is unknown (impedance distribution σ). The nonlinearity arises in σ, as the potential distribution ϕ is a function of the impedance, $\phi = \phi(\sigma)$, and we cannot easily solve Equation 4.2 for σ (Molinari 2003). The ill-posed nature of the problem is clearly apparent when observing the diffusive nature of electricity, coupled with the inherent measurement errors.

4.1.2 Research

The areas required to develop an effective EIT system can be separated into three main categories; electrode configuration and connection, data acquisition, and data processing. The latter two have been researched and developed in similar fields, particularly the medical field. Polydorides (2002) in particular has worked extensively in addressing the data processing issue of soft-field tomography, and has developed a MATLAB toolkit EIDORS exclusively for this problem.

The Electrical Impedance and Diffuse Optical Reconstruction Software (EIDORS) project has developed a community that promotes communication and sharing of software to further the development of EIT. The software, documentation, demonstrations and available help will be useful when data processing and volume visualization begins in this project.

As for the data acquisition system, the experiment of Weerld et al. (2001) required collecting data from 192 electrodes simultaneously to produce near real-time images, and did so successfully. However, the optimum order and procedure in collecting data has been debated by Molinari (2003) and Polydorides (2002), both of whom have modeled the system at hand extensively, but have performed little physical experimentation. Polydorides (2002) has suggested that a 16 electrode ring is the optimum size based upon computational time, the noise imposed by additional electrodes, and the fraction of singular values that are useful. Another method of interest suggested by Polydorides (2002) is a segmented electrode configuration. For example four electrodes across from one another would be turned on simultaneously, while the remaining electrodes measure voltage independently. Molinari (2003) and Polydorides (2002) have many suggestions on techniques to reduce computational time, increase resolution, and filter out noise, but all of this will be applied and discussed in greater detail when data acquisition begins.

The major foreseen difficulty is in the electrode configuration and connections. In several papers (Van Weereld et al., 2001, Polydorides 2002, and Molinari 2003) it has been found that accurate, consistently geometric connections are difficult to obtain, and the practical

limitations imposed by wiring limit the number attached by hand (Van Weereld et al. 2001). A solution to this problem was to use a flexible circuit designed for the core specifically to ensure consistent size and distribution of electrodes while also creating a compact manageable system as compared to conventionally wired electrodes. However, to begin the research a conventional wiring scheme has been used to begin testing some of the data collecting and processing schemes.

4.2 THE EIT APPARATUS

The primary idea behind the EIT apparatus, more specifically the electrode configuration, is that solid connections to the core sample must be made and the electrodes must be equidistant around the circumference of the core. This is in order to simplify the model used in solving the inverse problem. The design variations of the apparatus appear when trying to decide on a feasible number of electrodes, whether a flexible circuit is warranted and viable, and which design will be simple and reliable.

4.2.1 Electrode Design

The preliminary design decided upon is simple enough to eliminate many unnecessary problems, such as leaks from the system, short circuiting, and poor connections. Yet the system is large enough with 3 rings of 16 electrodes to test the data acquisition system and the MATLAB toolkit EIDORS in post processing. Figure 4.2 shows the preliminary design with 3 rings of 16 electrodes attached to the Berea sandstone core with conductive epoxy. This design will work by placing the base of the sandstone into water and allowing water to naturally imbibe by capillary forces. During this time the data acquisition system will be recording the field potential and calculating the internal impedance distribution. The idea is that visual observations of the saturation front can be used in assessing the EIT system and its performance.

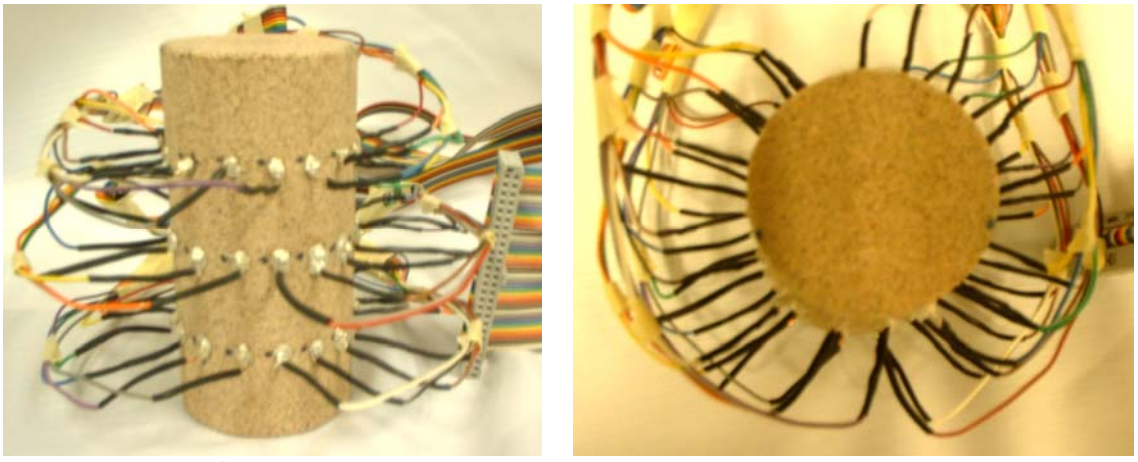

(Side View) (Top View)

Figure 4.2: Side and top view of Preliminary Design. 48 electrodes were attached to a Berea sandstone core using conductive epoxy.

If the preliminary design is successful in proving that it is feasible to determine saturation with EIT, then the project will move forward to one of the mentioned future designs. The

two foreseen options will allow for high pressure and temperature conditions along with pressurized phase transport through the core, just as in typical core experiments. However, the main point at which the designs diverge is whether to use a flex circuit design or a modified rubber sleeve design. These two options will be investigated as research continues.

4.2.2 Data Acquisition System

The basic requirments of the EIT data acquisition system were found to be very similar in the case of Polyrides, and Weereld. The EIT system requires a computer with sufficient speed and memory to handle the data, a constant current source, and a matrix/multiplexer system that can handle the array of electrodes. Essentially the system must have the capability of measureing the voltage potential at all electrodes, while applying a designated current across a select set of electrodes. The system must then change the set of electrodes applying current and measure the voltage potential at the remaining electrodes. It is obvious that under such a situation many measurments must be taken and a high speed switching system is nessesary. In our case with 48 electrodes, 2,304 switches need to be made. This is why National Instruments SCXI-1130 switch matrix was selected. The current numbering system for our core can be seen in figure 4.3.

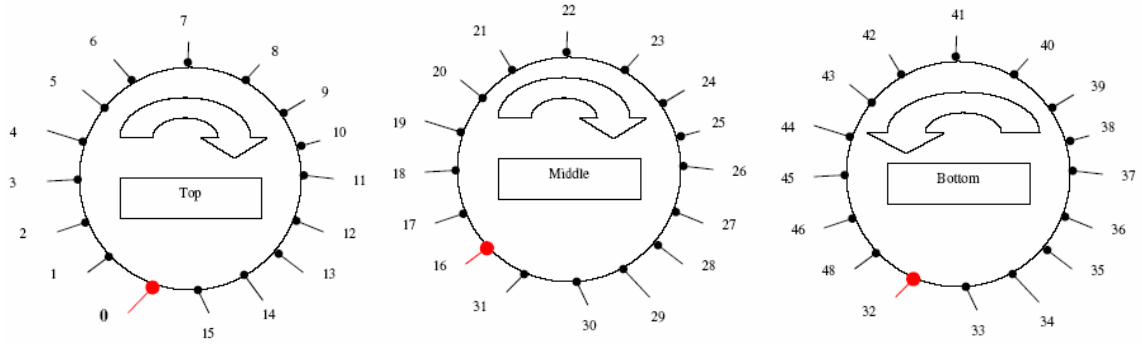

Figure 4.3: Numbering system for top, middle and bottom electrode plan.

The SCXI-1130 is set up in a 4x64 (1-wire) configuration, meaning that 64 channels are crossed with four channels, giving the ability to access 64 channels from 4 channels. The present design will be using 4x49 channels, 48 electrodes with one ground crossed with one current source channel and three voltage measurement channels. The SCXI-1130 has the capability of scanning at a rate of 900 cyles per second, which corresponds to an estimated scan time of 2.5 seconds for the 48 electrode core. With a scan rate this fast it is anticipated that it will be possible to capture saturation fronts traveling through the core and it may also be possibly to reduce the noise present in the data by performeing a time moving average.

The accuracy of our system is unknown at this point, but some limitations of our system are known. The National Instruments equipment has several important limitations, the applied current cannot exceed 400mA, and the voltage my not exceed 30 Vac, and the

switching rate is limited to 900 cycles/minute. These facts may or may not effect the experimement in the future, but will be kept in mind when designing test runs.

A schematic of the actual EIT apparatus can be seen in Figure 4.4. The matrix will be controlled by the VI developed in LABview on the PC. The voltage potential data will be aquired using LABview with the DAQ card. The collected data will then be processed in the MATlab program developed by the EIDORS project.

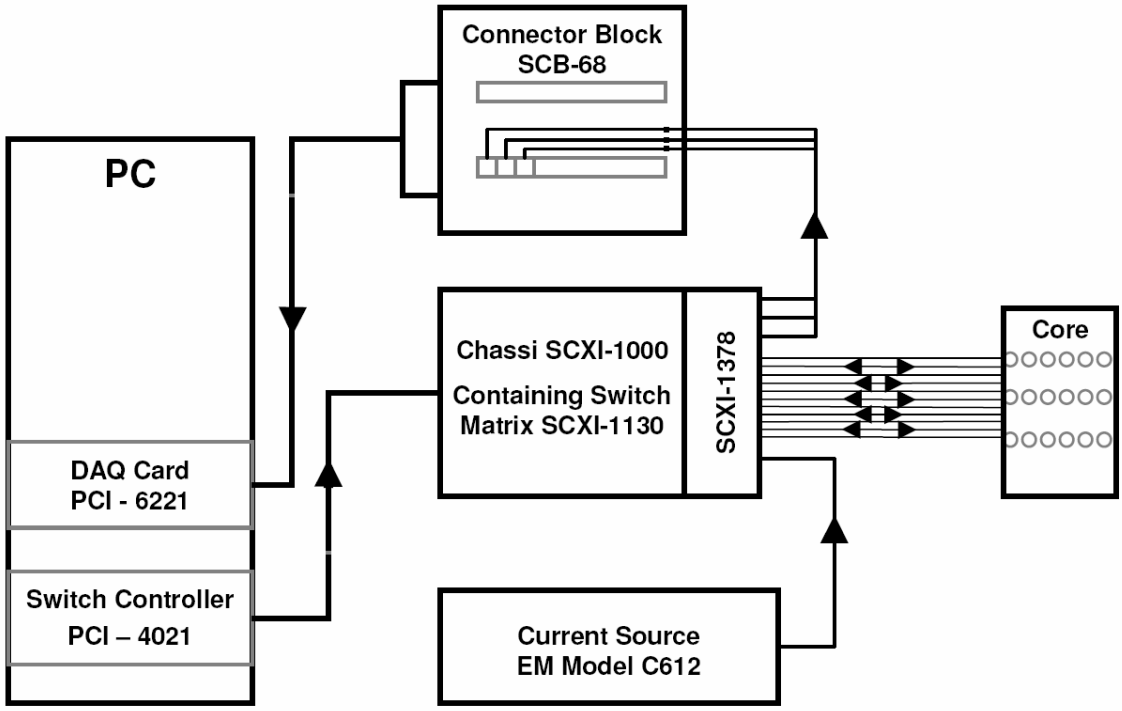

Figure 4.4: The present EIT system schematic. The PC cycles through the core through the switch matrix by measuring the voltage potential at every electrode before changing the current source electrodes. The current source is supplied by a constant current source, while the voltage potential measurements are retrieved by the DAQ card.

4.2.3 Data Processing

The data processing portion of the experiment has not been done with experimental data yet, but data generated in EIDORS demo project has been processed. (Figure 4.4) This demo consisted of a cylinder 3 units tall with a radius of 1 unit. Two rings of 16 electrodes are placed around the cylinder and a finite mesh created for this geometry is used. The resistivity coefficients in two areas are assigned in the finite mesh Figure 4.4 (a, b). This configuration is solved as a forward problem to generate the voltage potential measurements, where prior to being used to solve the inverse problem a factor to generate Gaussian noise in the data is applied. This is done to imitate actual experimental data, and allow for a feel for the effects of electrical noise. The inverse solution can be seen in

Figure 4.5 (c-l). The effects of electrical and numerical noise are observed clearly. The diffusive nature of the problem greatly reduces the detection of sharp contrasts in materials and this problem will be addressed through solution and measurement methods.

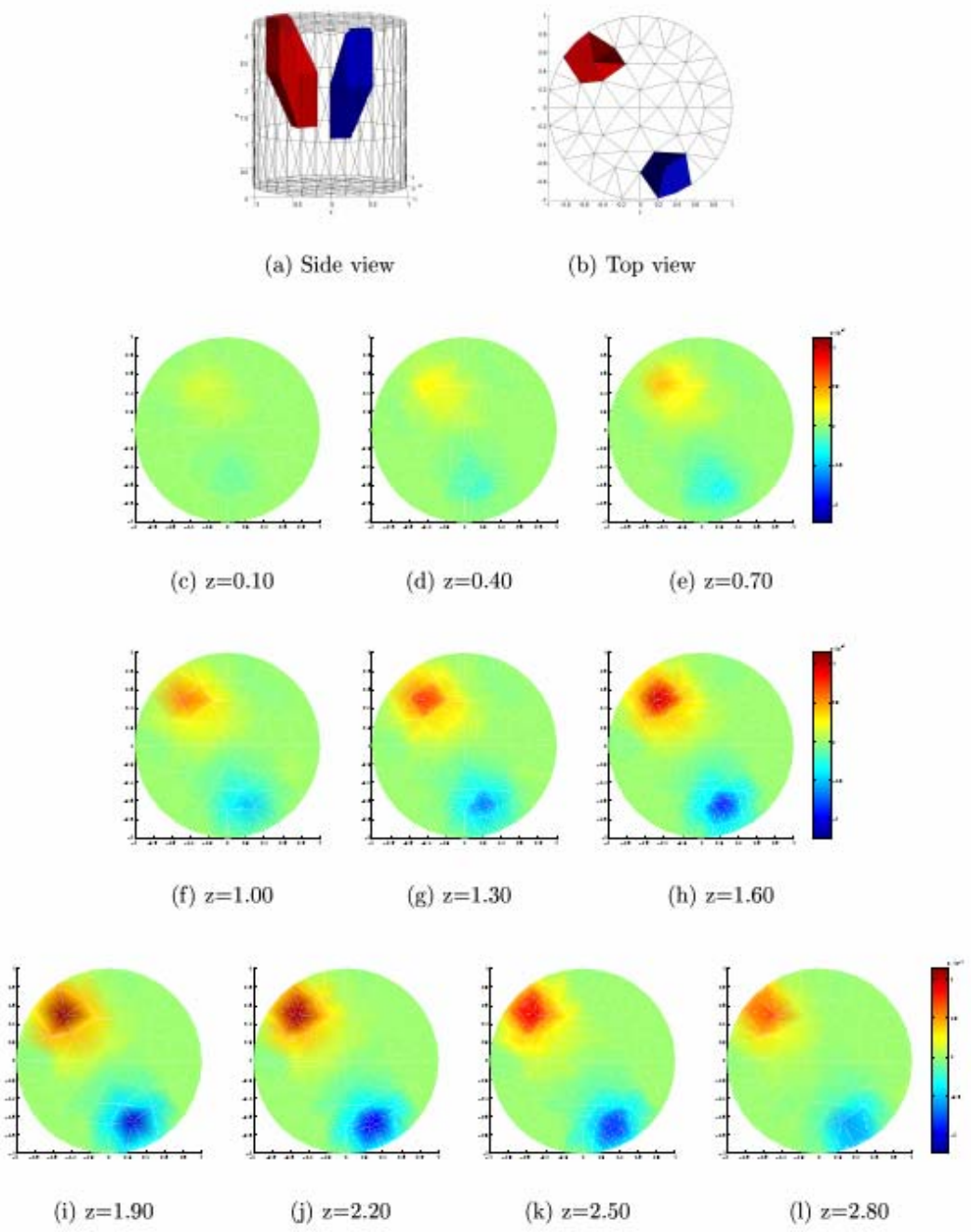

Figure 4.5: EIDORS demo program results. Images a and b are views of the cylinder core created with assigned resistivity values in two regions. This is used to generate the voltage potential data. Images c-l are cross sections of the inverse solution. (Polyrides 2002)

The inverse problem can be solved using two methods within EIDORS. The first approach is often called the Gauss-Newton method. It involves eliminating the second derivative in the Taylor expansion of the nonlinear forward problem, creating a generalized inverse of the Jacobian and inverting the well posed problem with the Newton-Raphson method. The second method considers a linearised form of the inverse problem and then adopts a Tikhonov type regularization to obtain a step solution within the Newton-Raphson method. (Polyrides 2002)

One step that Polyrides suggests that deserves attention is that of the finite element mesh used in solving the inverse problem. This demo program uses a relatively course mesh with 928 measurements. In our case we will be using approximately 2,300 measurements, increasing the computational time significantly. Therefore attention must be made in creating the mesh; the mesh density at the electrodes must increase to take into account the influence of the electrodes to reduce iterative solver time. However, the mesh will evolve with the rest of the experiment, always moving towards greater speeds and accuracy.

4.3 EXPERIMENTAL RESULTS

The approach used has been to perform small experiments systematically to ensure we understand how the equipment works, what values we should expect, and of course to find the problems in our system.

4.3.1 Preliminary Results

The preliminary results achieved thus far are promising and have shown that we are able to detect the saturation fronts caused by simple imbibition in the Berea sandstone core. These results were observed without solving the inverse problem. This was accomplished by simply applying a DC current across the core, and measuring the voltage potential at two electrodes during the imbibition process. The voltage potential increased drastically, from nearly 0 to 6 volts, as the saturation front reached the electrode plane. The change in voltage potential at each electrode corresponded with its distance away from the current applying electrodes, which was as anticipated for a relatively homogeneous medium, such as a partially saturated sandstone core.

This test proved that our equipment is functioning, a voltage was applied across the core to create a current, and the voltage potential around the core was measured giving evidence of saturation movement. However, the necessary conditions to solve the inverse problem were missing. The idea behind EIT is to bring the system to steady state, and take measurements on the surface that do not affect the steady-state condition. In our case our current source was actually a constant voltage source, therefore any voltage measurements changed the voltage potential field significantly. For that reason we now have replaced the function generator with a constant current source.

By implementing a constant current source several new issues arise, since we are now dealing with a much higher current, up to 400mA, the problem of induced signals in neighboring wires has appeared. The operation of the current generator alone, disconnected

from the system, creates an alternating voltage signal on the order of several volts. To address this problem we are presently trying to shorten the leads from the core to minimize induction potential, shield the system from the current generator, and examining the noise caused by the labs lighting.

4.4 CONTINUING AND FUTURE WORK

Currently we are working to address the issue of induced signals as mentioned above without the noise removed visualization of any accuracy will be impossible. However, the LABview VI for the system has been written and should be able to begin collecting quality data as soon as the noise in the signals is removed. This data will then be processed in the EIDORS Matlab package for visualization, after the finite element grid for the core has been constructed.

There are several long term goals for the project one is to verify saturation measurements obtained with the EIT system with CT scanner saturation measurements. Another future goal is to implement a high pressure and temperature column so that experiments at reservoir conditions can be performed.

5. FRACTURED ROCK RELATIVE PERMEABILITY

This project is being conducted by Research Assistant Anson L. Villaluz, Senior Research Engineer Kewen Li and Prof. Roland N. Horne. The objective is to obtain measurements of steam-water relative permeability in real fractured rocks from geothermal reservoir. This work is an extension of our earlier steam-water relative permeability studies which have mostly considered artificially uniform and high permeability rocks. Having understood the mechanisms of relative permeability, we embarked on the more difficult measurements using heterogeneous, low permeability rocks from geothermal reservoirs. This task was completed this quarter and a technical report issued.

5.1 BACKGROUND

Steam-water relative permeability and capillary pressure are important data for geothermal reservoir engineering. The Stanford Geothermal Program (SGP) has succeeded in making fundamental measurements of steam-water flow in porous media and made significant contributions to the industry. One of the important problems left to undertake is the measurement of steam-water relative permeability and capillary pressure in fractured, low permeability geothermal rock, as most of the previous study was conducted in high permeability sandstone as a well-controlled test material.

We have concluded from earlier experimental data (Satik, 1998; Horne *et al*., 2000; Mahiya, 1999; O'Connor, 2001; Li and Horne, 2000) that steam-water relative permeability of porous medium follows the Corey model and steam-water capillary pressure follow the Brooks-Corey model. We can measure the end-point steam-water relative permeability and saturation in the geothermal rock with permeability smaller than 1 md using the resistivity method (Archie's equation) and/or the direct weighing method developed by Li *et al*. (2001). Then the whole curve of steam-water relative permeability can be obtained using the Corey model and the capillary pressure curve can be obtained using the Brooks-Corey model. We confirmed the applicability of this approach first with nitrogen-water experiments, which are easier to conduct than the steam-water flows. Now, we want to investigate relative permeability in real fractured rocks. This work was begun by Habana (2002), who ran into experimental difficulties and was not able to complete the measurements.

A lot of work has been done to study flow behavior in nonfractured porous media; some experiments have also studied flow behavior in synthetic fabricated fractures. This study used a core sample from The Geysers geothermal field.

Understanding liquid-gas flow properties in real fractured rock will enable us to do production forecasts through numerical simulations more accurately. This will lead to better information for decision making regarding reservoir management and development.

5.2 EXPERIMENTAL METHODOLOGY

In this report, details regarding the experimental design which enabled measurements of parameters necessary for determining relative permeability are discussed. Two types of experiments were particularly designed for, one is the steady-state relative permeability measurement of Berea sandstone and another is the steady-state relative permeability measurement of a geothermal rock. Some preliminary experiments were also done before the relative permeability measurements were performed, and these are also described in this chapter.

5.2.1 Experimental apparatus

Berea Sandstone

Parameters necessary to establish relative permeability curves are pressure, flowrate and saturation. Pressure transducers were used to measure pressure drop and outlet pressure, a 200 cc/min Matheson Flow Meter was used to determine flowrate, two balances were used to measure and cross validate saturation data. An RCL meter (AC) was also used to measure resistance along the core during experiments.

The main component of the system was a 2 inch diameter Berea sandstone core that is 4 inches in length, with an absolute permeability of about 680 md and a porosity of 22.7%.

An aluminum core holder was used to provide boundary for fluid flow (with confining pressure) and mechanical support. Rubber sleeve with heat shrink tubing atop was used to separate the core from the confining pressure. 100 psi confining pressure was applied and pressure drop across the core ranged from 1.5 – 5 psig during the steady state relative permeability experiments.

Geothermal Rock

The main challenges in dealing with geothermal rock were its low permeability and its low porosity values. Because of these, experiments must be done at high pressures. A 500 psi pressure transducer was used to measure pressure drop, while a 25 psi pressure transducer measures the outlet pressure, an RCL meter (AC) and one balance (for output) were used to measure and cross validate saturation. Gas flow rates were measured using the volume displacement method with an inverted graduated cylinder, water, and a stopwatch.

Figure 5.1 is a schematic of the apparatus that allows real-time measurement of the required parameters. The main component of the system was a 2.72 inches geothermal rock that is 1.86 inches in length, the core was obtained from a depth of 2440.5 m at The Geysers geothermal field, a picture of the core assembly can be seen in Figure 5.2. It has an absolute permeability of around 0.7 md at a confining pressure of 550 psi and a porosity of 1.7%.

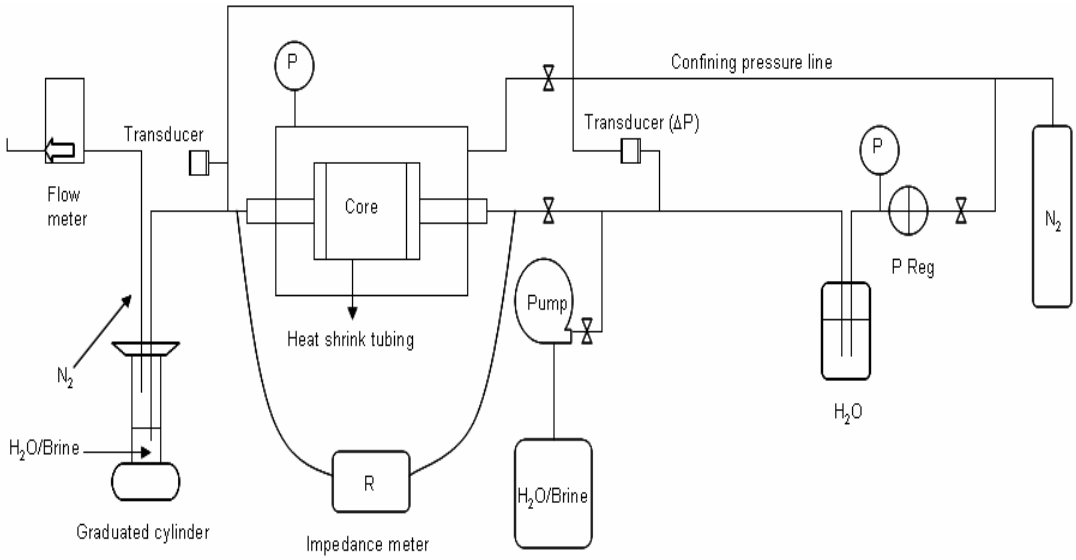

Figure 5.1: Experimental setup for nitrogen-water relative permeability in fractured rock

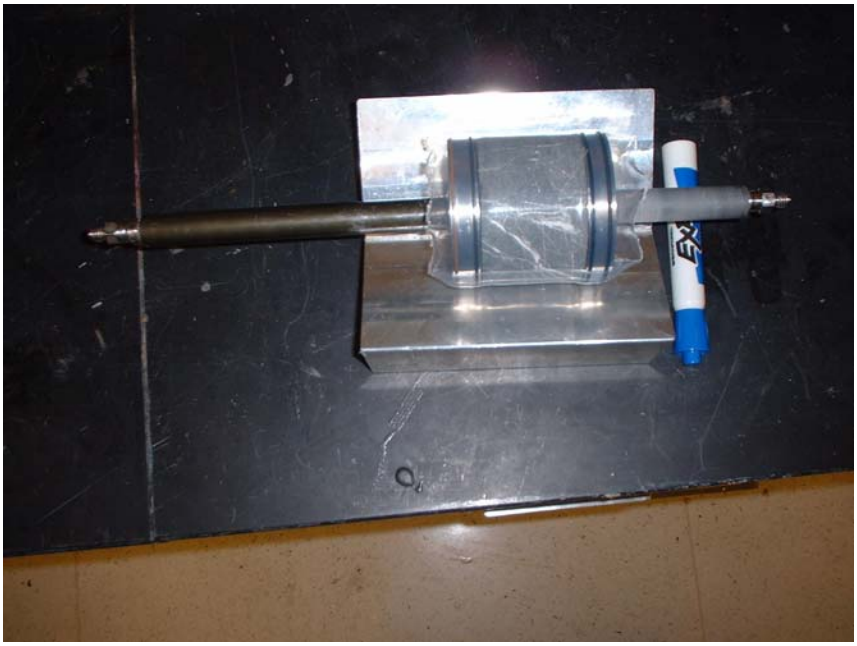

Figure 5.2: Photo of the geothermal core with shrink tubing and end plates

The aluminum core holder used for Berea sandstone would not stand the high pressure, therefore, a stainless steel core holder was used. Heat shrink tubing was used to separate the core from the confining pressure. Figure 5.3 is a picture of the experimental system.

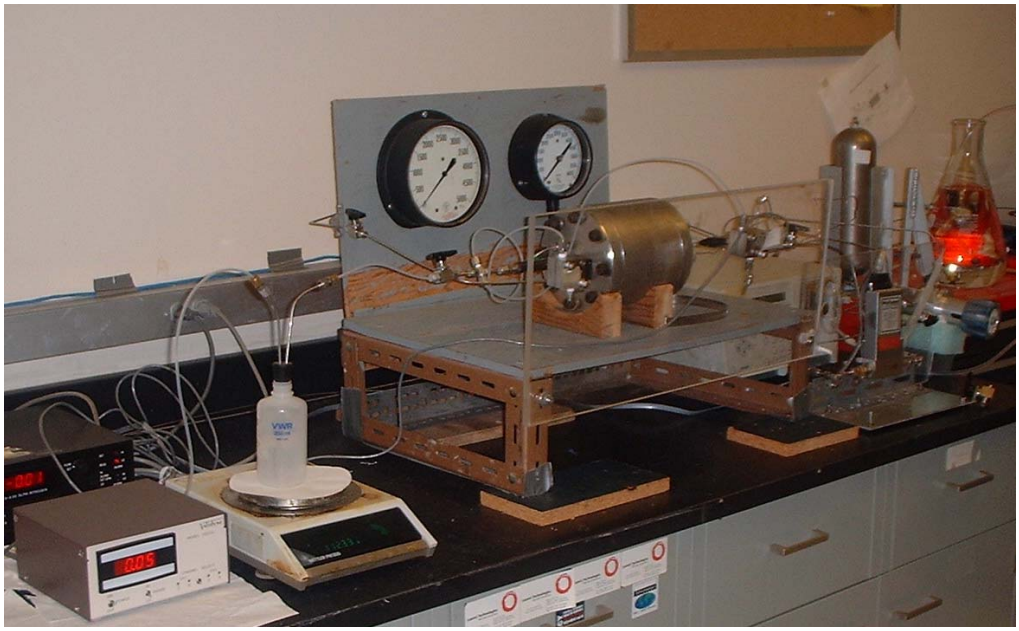

Figure 5.3: Photo of the experimental system.

5.2.2 Absolute Permeability

Berea Sandstone

Permeability was determined by brine (1% NaCl) injection, three brine injection experiments were conducted. Flowrate was maintained constant for each experiment at 5 ml/min. Steady state was deemed achieved when the pressure drop was relatively constant. Outlet pressure was maintained at atmospheric pressure.

Geothermal Rock

Permeability was determined by brine (1% NaCl) injection, two brine injection experiments were conducted. Flowrate was maintained constant for each experiment at 0.3 ml/min, and another run at 0.4 ml/min. The data acquisition system was automated for taking pressure drop measurements.

5.2.3 Klinkenberg Effect

Slip effect was studied in the geothermal rock by measuring gas permeability at room temperature. Flow measurements were conducted at a series of different mean pressures and different confining pressures ranging from 400 to 800 psig. Three nitrogen experiments were completed for the geothermal rock after drying the core at 110^{o}C while pulling a vacuum.

5.2.4 Resistivity Experiments

Berea Sandstone

Resistance measurements at different AC frequencies were taken while doing the three steady state drainage and imbibition relative permeability tests on the core. Experiments were also done measuring resistance of the core while letting the saturated core dry naturally. 1 % NaCl brine was used for all the experiments. The apparatus for this experiment is shown in Figure 5.4; a sample photo is shown in Figure 5.5. In all of these experiments, saturation was also measured using the weighing method.

Geothermal Rock

Resistivity-saturation correlation was gotten while evaporating the core naturally, 1% NaCl brine was used as the saturating liquid. Resistances at frequencies ranging from 100 Hz to 100 kHz were recorded. Resistance measurements were also documented while doing the flow experiments, making sure that the end plates were well insulated with the metallic core holder. The measurements were then used to infer saturation on steady state.

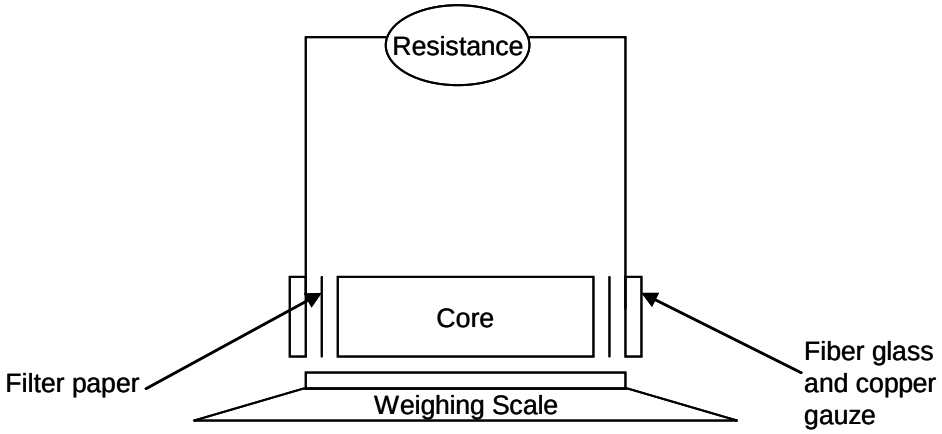

Figure5.4: Apparatus for determining resistivity-saturation correlation

Figure 5.5: Photograph of resistivity-saturation correlation experiment apparatus

5.3 EXPERIMENTAL RESULTS AND DISCUSSION

5.3.1 Absolute Permeability

Water Injection in Berea Sandstone

Table 5.1 summarizes the results from three experiment runs performed. The Berea sandstone used has an average absolute permeability of about 684 md.

Table 5.1: Absolute permeability results for Berea sandstone

Flow rate (ml/min)	permeability (md)
5	681
5	681
5	690

Water Injection in Geothermal Rock

Table 5.2 summarizes the results from two experiment runs performed under a confining pressure of 550 psi. The flow experiment took around 50 hrs to reach a stable pressure. Two more water injection experiments were done before those presented in Table 5.2, the permeability values gotten for these were considerably lower possibly due to trapped gas. The core was then evacuated to solve the problem.

Table 5.2: Absolute permeability results for geothermal rock

Flow rate (ml/min)	permeability (md)
0.3	0.6844
0.4	0.696

The absolute permeability values obtained by Habana (2002) were also less than 1 md. This past work showed that permeability of the core used was around 0.2 to 0.3 md. The permeability of the core used in this research is higher probably due to the presence of more visible fractures.

5.3.2 Klinkenberg Effect

Figure 5.6 shows the results of three nitrogen experiments performed on the geothermal rock. Absolute permeability can be determined taking into account slip effect by extrapolating permeability data to the ordinate axis. Absolute permeability at 550 psi of confining pressure was determined to be around 0.7 md. This value verifies the absolute permeability values obtained through water injection shown in Table 5.2. Meanwhile, Table 5.3 summarizes slip factors calculated for these experiments.

It can also be observed that as confining pressure increases, absolute permeability decreases. This can be attributed to decrease in fracture aperture due to increased net stress, consequently decreasing permeability.

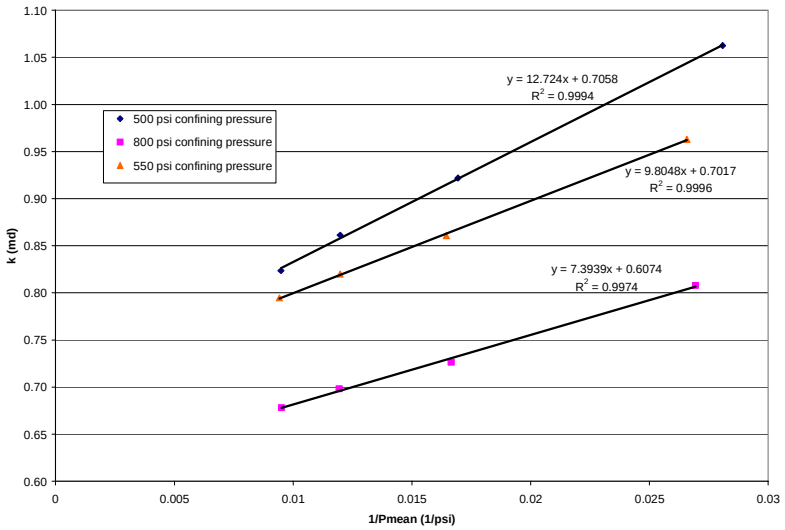

Figure 5.6: Results of geothermal rock Klinkenberg effect using nitrogen gas

Table 5.3: Calculated slip factor at 550 psi confining pressure

550 psi confining pressure		
effective permeability	mean pressure (psi)	b (atm^{-1})
0.96	37.62	0.95
0.86	60.80	0.94
0.82	83.47	0.96
0.79	106.14	0.96
Ave:		**0.95**

5.3.3 Nitrogen-Water Relative Permeability

Berea Sandstone

Table 5.4 summarizes the results for nitrogen-water relative permeability measurements for the porous medium used and Figure 5.7 is a plot of these results.

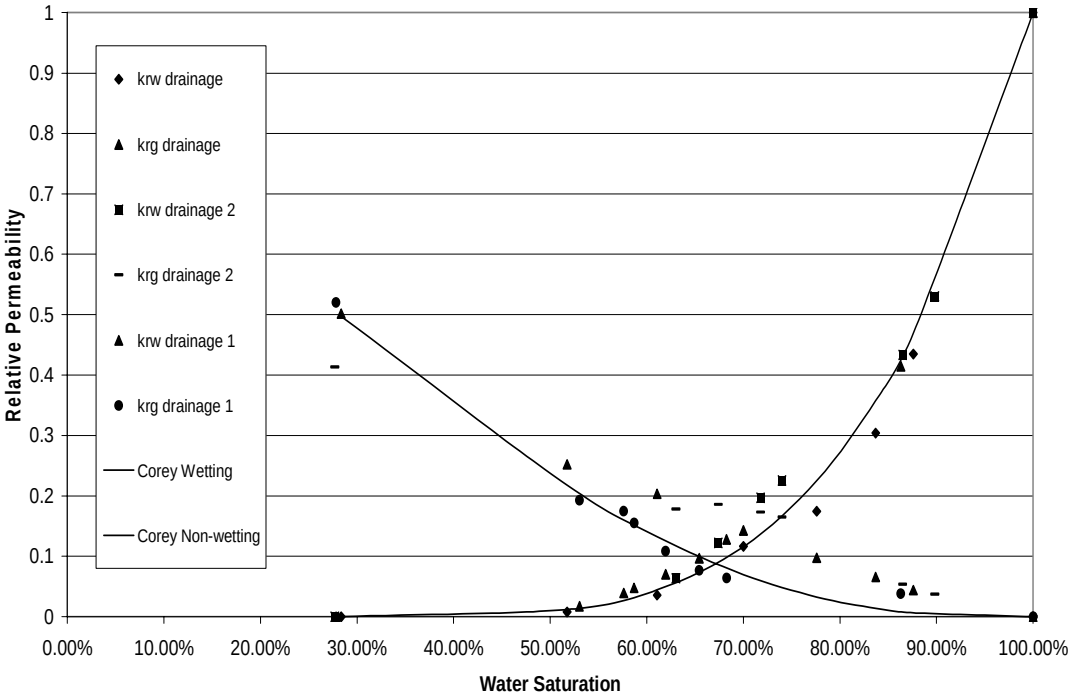

Figure 5.7: Nitrogen-water drainage relative permeability in a porous media

The general trend of the results seen in Figure 5.7 is acceptable. Relative permeability of a particular phase increases as saturation of that particular phase increases and vice versa. Plotted against a semiempirical model, the results can be observed to generally follow the Corey series model (Brooks-Corey model with $\lambda=2$, where λ is the pore size distribution index). Past researchers also had similar results and it is generally accepted that nitrogen-water relative permeability in porous media follows the Corey model.

On the other hand, Figure 5.8 presents the results during the imbibition process. The results generally follow the trend expected. Resistivity tests were done while doing these experiments and results from these measurements will be discussed in a later section.

Table 5.4: Tabulated results for nitrogen-water relative permeability in Berea sandstone

Drainage		
Sw	krw	kg
100.00%	1.0000	0.0000
87.61%	0.4351	0.0441
83.69%	0.3040	0.0658
77.60%	0.1747	0.0977
69.99%	0.1164	0.1430
61.08%	0.0359	0.2035
51.73%	0.0079	0.2524
28.35%	0.0000	0.5019
Drainage 1		
Sw	kw	kg
100.00%	1.0000	0.0000
89.80%	0.5304	0.0372
86.48%	0.4337	0.0535
73.99%	0.2256	0.1650
71.78%	0.1969	0.1733
67.41%	0.1223	0.1860
63.01%	0.0636	0.1782
27.68%	0.0000	0.4136
Drainage 2		
Sw	krw	kg
100.00%	1.0000	0.0000
86.30%	0.4146	0.0384
68.25%	0.1279	0.0638
65.43%	0.0970	0.0768
61.95%	0.0702	0.1086
58.69%	0.0477	0.1549
57.60%	0.0392	0.1747
53.03%	0.0173	0.1927
27.81%	0.0000	0.5201

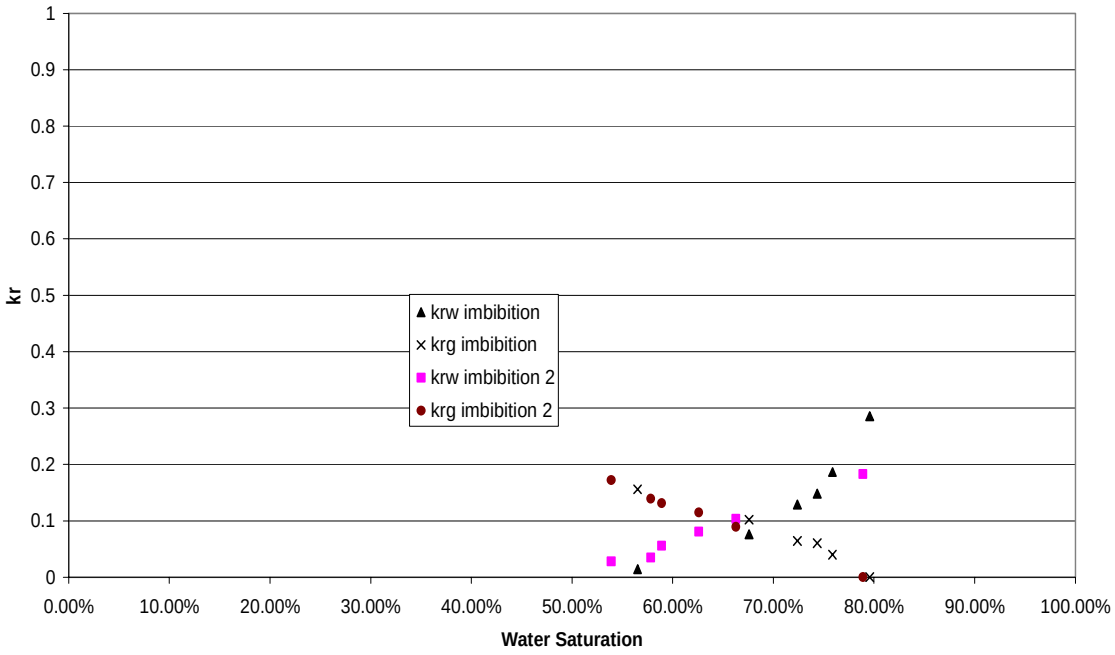

Figure 5.8: Nitrogen-water imbibition relative permeability in a porous medium

Geothermal Rock

Table 5.5 summarizes the results for nitrogen-water relative permeability measurements for the geothermal rock and Figure 5.9 is a plot of these results. Meanwhile, Table 5.6 tabulates the end point saturations after drainage and imbibition, saturations were determined using the weighing method.

Table 5.5: Tabulated results for nitrogen-water relative permeability in geothermal rock

Sw	Sw*	krw	krg
100.00%	1.0000	1.0000	0.0000
80.31%	0.4591	0.0884	0.2411
75.23%	0.3196	0.0590	0.3680
63.60%	0.0000	0.0000	0.7959

Table 5.6: End point residual saturations after drainage and imbibition

	Sw	Sg
Drainage end point	63.60%	36.40%
Imbibition end point	80.79%	19.21%

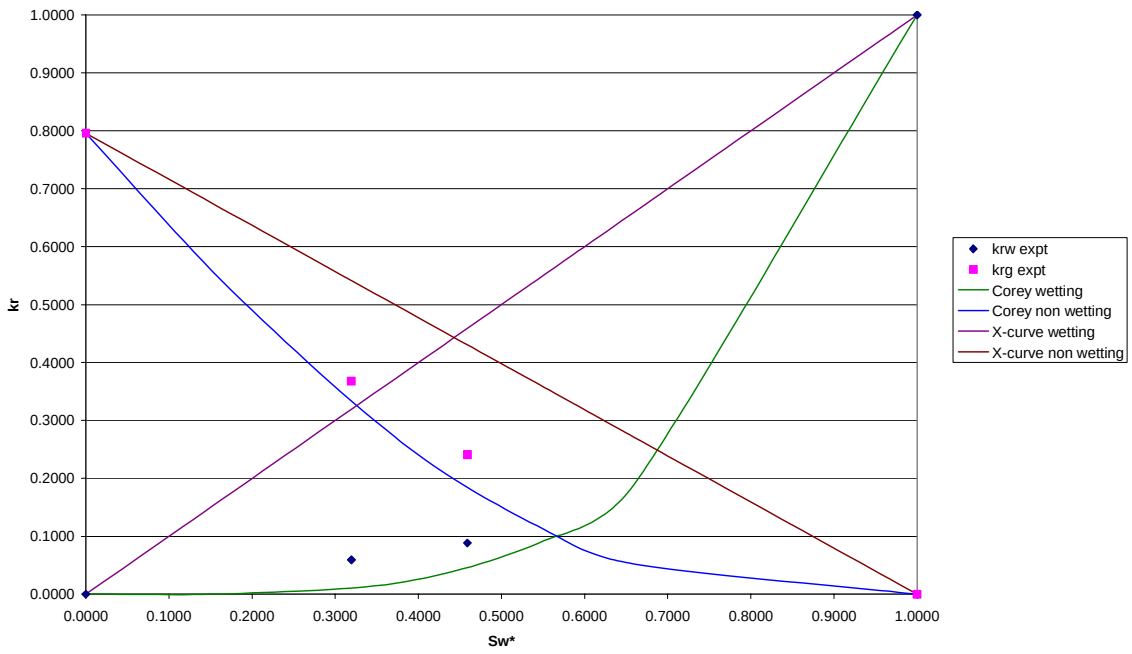

Figure 5.9: Nitrogen-water drainage relative permeability in a geothermal rock

Only four relative permeability points were measured due to the time constraint. As can be seen in Figure 5.9, relative permeability points measured for geothermal rock are quite different from that of a porous medium as they neither follow the Corey curves nor the X-curves. The results can be observed to be lower than the X-curves but higher than the Corey curves.

X-curve results from no phase interference usually due to flow to relatively big fractures. The Corey model is for flow of fluids through rock matrix and due to the relatively small pore size of the matrix, there is very substantial phase interference occurring (which is taken into account by the model). On the other hand, in fractured rocks, there is fluid flow through fractures as well as the rock matrix. Taking these arguments into account, having a relative permeability curve that is in between the two known models makes sense.

Furthermore, it can be observed in Figure 5.9 that the relative permeability points measured are nearer the Corey curves than the X-curves. This can probably be attributed to small aperture fractures of the geothermal rock. The X-curve inherently assumes that fractures are large such that there will be not much interaction between the two phases. It can be imagined that as the fracture aperture becomes smaller, the flow medium approaches properties of a capillary tubing and relative permeability of porous medium is usually modeled from flow through a bundle of capillary tubes.

5.3.4 Resistivity

Berea Sandstone

Figure 5.10 is a plot of results obtained from the resistivity studies performed while evaporating the core naturally as well as while flow experiments were being performed. 100 Hz of AC current was used for this experiment as results derived from this frequency fits Archie's correlation best during the preliminary natural evaporation experiment.

It can be observed from Figure 4-5 that all drainage, natural evaporation, and imbibition processes resulted in good Archie's correlation between saturation and resistivity at 100 Hz AC frequency. It is noteworthy that the cementation factor determined is higher (about 5.4) than that of the usual Berea sandstone's (about 2). This can possibly be attributed to the firing of the Berea sandstone used in the experiment. During the firing process, clays (which are conductive materials) are calcined, therefore, decreasing the overall conductivity of the material and increasing its resistance.

Another interesting observation from Figure 5.10 is that resistivity index seemed to be a function of flow history. For the imbibition process, indices were lower than that of the drainage process.

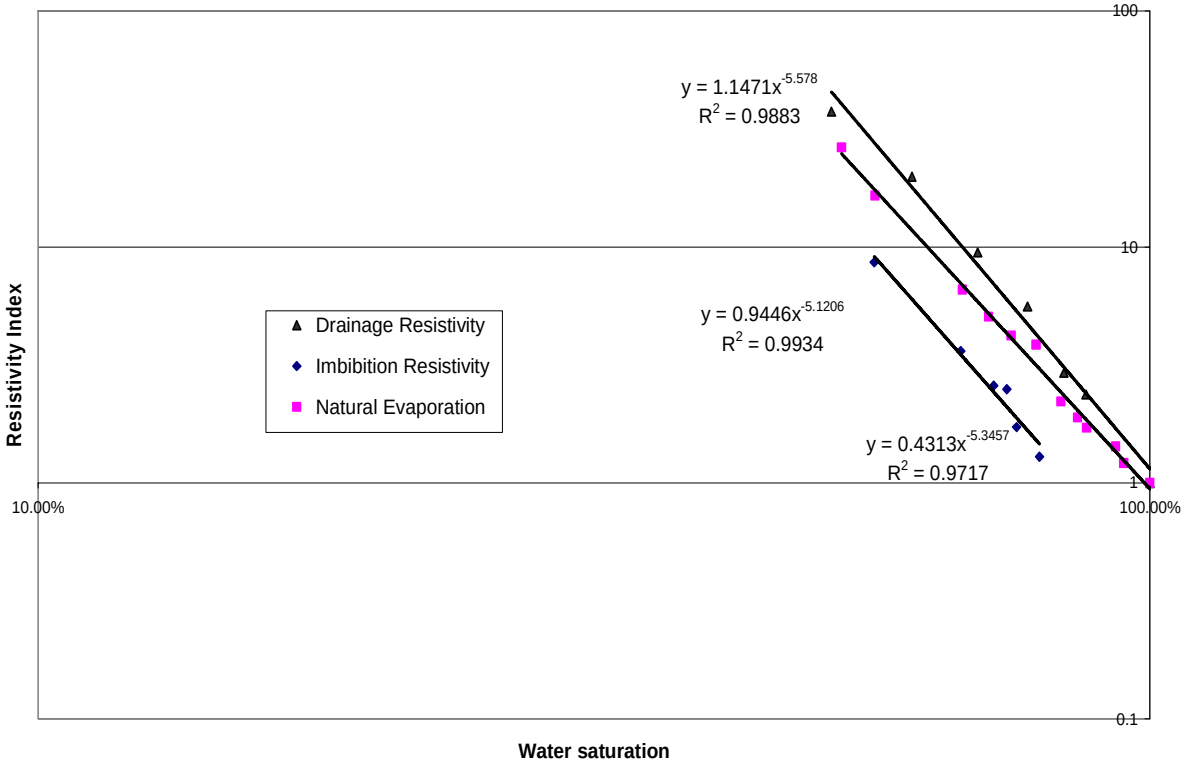

Figure 5.10: Resistivity studies results during drainage and natural evaporation of Berea sandstone

Geothermal Rock

A correlation between resistivity index and saturation was determined for the geothermal rock. This correlation was used to measure saturation during the relative permeability experiments. Several AC frequencies were used and it was found out that 10 kHz of frequency is ideal for geothermal rock. Results of tests using different frequencies are presented in Figures 5.11 to 5.14.

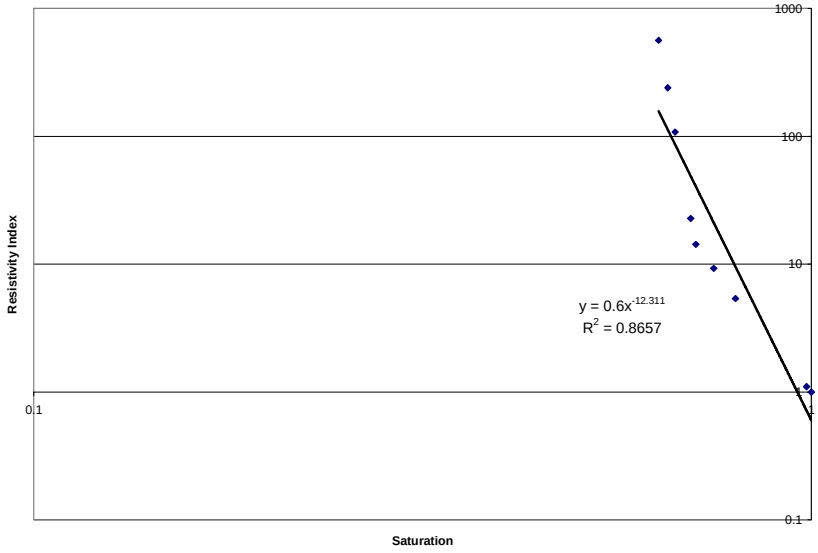

Figure 5.11: Resistivity index vs saturation at 100 Hz AC frequency

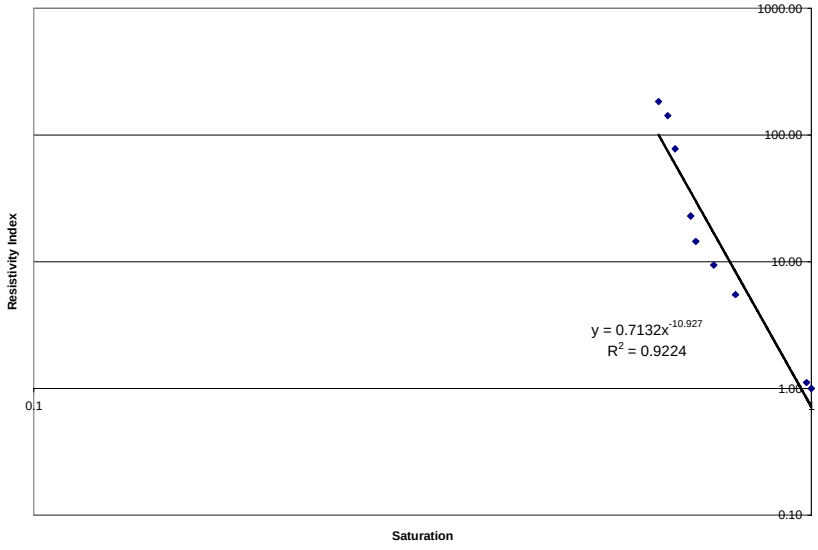

Figure 5.12: Resistivity index vs saturation at 1 kHz AC frequency

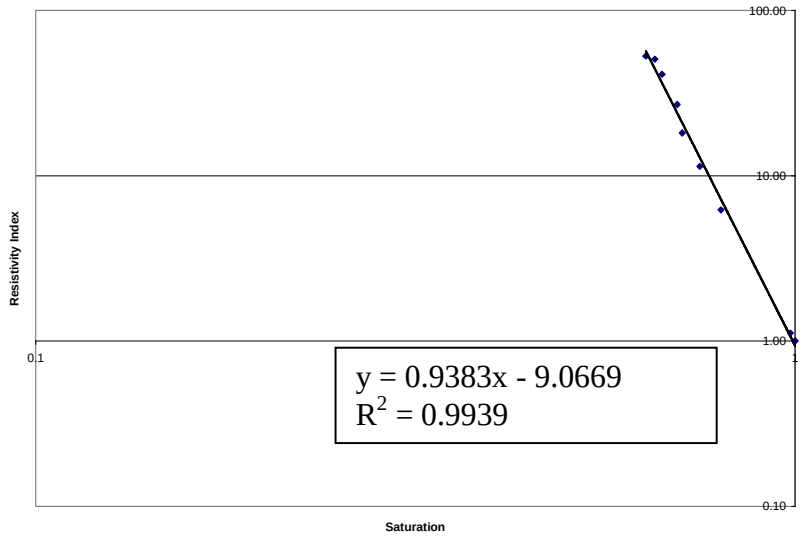

Figure 5.13: Resistivity index vs saturation at 10 kHz AC frequency

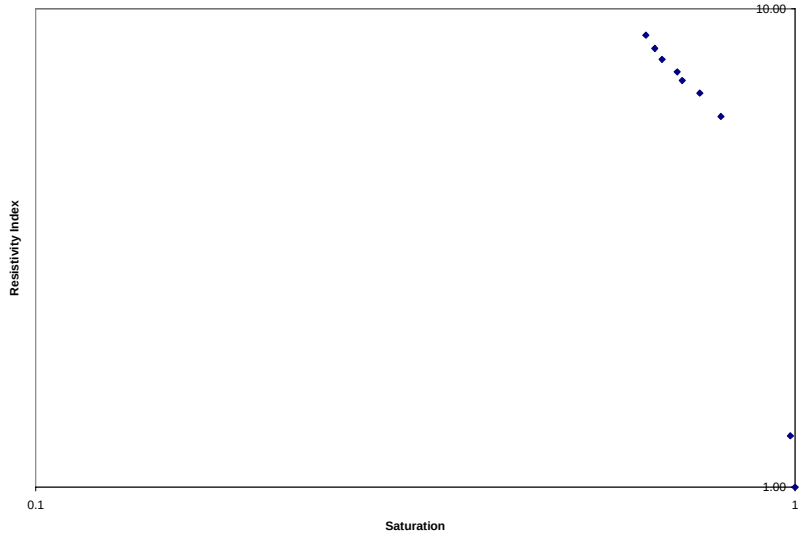

Figure 5.14: Resistivity index vs saturation at 100 kHz AC frequency

The experiment was done by allowing the saturated geothermal rock to evaporate naturally while taking measurements of weight and resistivity as time progressed. This experiment lasted until the resistance went outside the sensitivity of the RCL meter used. The lowest saturation value was around 60%. This result coincides with the end-point drainage saturation of 63.6%.

Lastly, through comparison of Figures 5.11 to 5.14, it can be observed that 10 kHz of AC frequency yields the best Archie's correlation between saturation and resistivity index. This was the correlation used to determine saturation from resistance data.

6. REFERENCES

Belen, R.P., Jr. and Horne, R.N.: "Inferring In-Situ and Immobile Water Saturations from Field Measurements", Geothermal Resources Council *Transactions* **24** (2000).

Chen, C.-Y.: *Liquid-gas relative permeabilities in fractures: effects of flow structures, phase transformation and surface roughness*, Ph.D. dissertation, Stanford University, Stanford, California, June 2005.

Chen, C.Y., Dastan, A., Juliusson, E., Horne, R.N., Li, K., Stacey, R.W. and Villaluz, A.L.: "Quarterly Report for Contract DE-FG36-02ID14418, Stanford Geothermal Program, January-March 2005," Stanford University, 2005.

Chen, C.-Y., Horne, R.N., and Fourar, M.: "Experimental Study of Liquid-Gas Flow Structure Effects on Relative Permeabilities in a Fracture," *Water Resources Research*, (Aug 2004), Vol. 40, No.8, W08301.

Corey, A.T.: *Mechanics of Immiscible Fluids in Porous Media*, Water Resources Publications, Littleton, Colorado (1986).

Fourar, M., and Lenormand, R.: "A Viscous Coupling Model for Relative Permeabilities in Fractures," SPE 49006, paper presented at the 1998 SPE Annual Technical Conference and Exhibition, New Orleans, Louisiana, USA, September 27-30.

Fourar, M., Bories, S., Lenormand, R., and Persoff, P.: "Two-Phase Flow in Smooth and Rough Fractures: Measurement and Correlation by Porous-Medium and Pipe Flow Models," *Water Resources Research* (November 1993) Vol. 29 No. 11, pp. 3699-3708.

Grant, M.A.: "Permeability Reduction Factors at Wairakei," *Proceedings*, AIChE-ASME Heat Transfer Conference, Salt Lake City, Utah, pp 15-17, August 1977

Guðmundsson, J.S. "Gas/Liquid Flow Metering by Pulse Testing," Department of Petroleum Engineering and Applied Geophysics, Norwegian University of Science and Technology, Trondheim. Available from internet: URL: http://www.ipt.ntnu.no/~jsg/forskning/forskning.html#Metering

Habana, M.D.: "Relative Permeability of Fractured Rock", MS report, Stanford University, Stanford, California, (2002).

Horne, R.N., Reyes, J.L.P., Li, K.: "Estimating Water Saturation at The Geysers Based on Historical Pressure and Temperatue Production Data by Direct Measurement," Final Report to California Energy Comission, June 2003.

Horne, R.H., Satik, C., Mahiya, G., Li, K., Ambusso, W., Tovar, R., Wang, C., and Nassori, H.: "Steam-Water Relative Permeability," Proc. of the World Geothermal Congress 2000, Kyushu-Tohoku, Japan, May 28-June 10, 2000.

Li, K. and Horne, R.N. (2000): "Steam-Water Capillary Pressure," SPE 63224, presented at the 2000 SPE Annual Technical Conference and Exhibition, Dallas, TX, USA, October 1-4, 2000.

Li, K. and Horne, R.N.: "An Experimental and Theoretical Study of Steam-Water Capillary Pressure," *SPEREE* (December 2001), p.477-482.

Li, K and Horne, R.N., Direct Measurement of In-Situ Water Saturation in The Geysers Rock, SU workshop, Jan. 2003.

Li, K., Nassori, H., and Horne, R.N. (2001): "Experimental Study of Water Injection into Geothermal Reservoirs," to be presented at the GRC 2001 annual meeting, August 26-29, 2001, San Diego, USA; *GRC* Trans. V. **25**.

Mahiya, G.: "Experimental Measurement of Steam-Water Relative Permeability," MS report, Stanford University, Stanford, California (1999).

Molinari, M.: *High Fidelity Imaging in Electrical Impedence Tomography*, Ph.D. dissertation, University of Southampton, Southampton, United Kingdom (2003).

Ning, X., The measurement of matrix and fracture properties in naturally fractured low permeability cores using a pressure pulse method, Ph.D. Thesis, Texas A&M, December 1992, published as Gas Research Institute Report GRI-93/0103, March 1993.

Nomura, M. "Integrated Analysis of Production and Wireline Logs," presented at SUPRI-D Affiliate Meeting, Stanford University, 2005.

O'Connor, P.A.: "Constant-Pressure Measurement of Steam-Water Relative Permeability," MS report, Stanford University, Stanford, California (2001).

Persoff P. and Hulen J. B. "Hydrologic characterization of four cores from the Geysers coring project" Proceedings of the 21st workshop on Geothermal Reservoir Engineering Stanford University Jan 22-24 1996 p.327-333

Phogat V. K. and Aylmore L. A. G. "Computation of hydraulic conductivity of porous materials using computer assisted tomography." Aust. J. Soil. Res. 24, 071-8, 1996

Polydorides, N.: *Image Reconstruction Algorithms for Soft-Field Tomography*, Ph.D. dissertation, University of Manchester, Manchester, United Kingdom (2002).

Reyes, J.L.P., Chen C.-Y., Li, K., and Horne, R.N.: "Calculation of Steam and Water Relative Permeabilities Using Field Production Data, with Laboratory Verification," *Geothermal Resources Council Transactions* (2004), Vol. 28, pp. 609-615.

Reyes, J.L.P., Li, K., and Horne, R.N.: "Estimating Water Saturation at The Geysers Based on Historical Pressure and Temperature Production Data and By Direct Measurement," *Geothermal Resources Council Transactions* (2003), Vol. 27, pp. 715-726.

Sanyal, S.K.: "Estimation of Steam Saturation and Rock Alteration from Geothermal Well Logs - A Theoretical Inquiry", *Geothermal Resources Council Transactions* (1981).

Satik, C.: “A Measurement of Steam-Water Relative Permeability,” Proceedings of 23rd Workshop on Geothermal Reservoir Engineering, Stanford University, Stanford, California (1998).

Shinohara, K., “Calculation and Use of Steam/Water Relative Permeabilities in Geothermal Reservoirs”, MS report, Stanford University, Stanford, California (1978).

van Weereld, J.J.A., Player M.A., Collie, D.A.L, Watkins, A.P., Olsen, D.: “Flow Imaging in Core Samples by Electrical Impedance Tomography,” paper SCA 2001-06, Society of Core Analysts.